

Causal Inference in Biomedical Imaging via Functional Linear Structural Equation Models

Ting Li

School of Statistics and Data Science,

Shanghai University of Finance and Economics, Shanghai, China

Ethan Fan

Department of Biostatistics, Duke University, Durham, USA

Tengfei Li and Hongtu Zhu*

Departments of Radiology, Computer Science, Genetics, and Biostatistics,
University of North Carolina at Chapel Hill, Chapel Hill, USA

Abstract

Understanding the causal effects of organ-specific features from medical imaging on clinical outcomes is essential for biomedical research and patient care. We propose a novel Functional Linear Structural Equation Model (FLSEM) to capture the relationships among clinical outcomes, functional imaging exposures, and scalar covariates like genetics, sex, and age. Traditional methods struggle with the infinite-dimensional nature of exposures and complex covariates. Our FLSEM overcomes these challenges by establishing identifiable conditions using scalar instrumental variables. We develop the Functional Group Support Detection and Root Finding (FGS-DAR) algorithm for efficient variable selection, supported by rigorous theoretical guarantees, including selection consistency and accurate parameter estimation. We further propose a test statistic to test the nullity of the functional coefficient, establishing its null limit distribution. Our approach is validated through extensive simulations and applied to UK Biobank data, demonstrating robust performance in detecting causal relationships from medical imaging.

Keywords: Causal Effect; Functional Linear Structural Equation Model; Identification; Imaging Genetics; Instrumental Variable.

*Address for correspondence: Hongtu Zhu, Ph.D., E-mail: htzhu@email.unc.edu.

1 Introduction

This paper proposes the Causal-Genetic-Imaging-Clinical (CGIC) framework to uncover causal pathways linking genetic factors, organ-level imaging markers, and clinical outcomes for complex phenotypes such as Alzheimer’s Disease (AD), while accounting for environmental influences and unobserved confounders (Zhu et al., 2023; Le and Stein, 2019; Taschler et al., 2022). Imaging modalities like functional Magnetic Resonance Imaging (fMRI) play a central role in capturing anatomical and functional properties of organs such as the brain (Zhou et al., 2021). The CGIC framework extends Jack’s influential hypothetical model of AD progression (Jack Jr et al., 2010, 2013), offering a more comprehensive view of disease etiology (Figure 1(a)). Large-scale studies such as the Alzheimer’s Disease Neuroimaging Initiative (ADNI) provide critical multimodal data for investigating the interplay among genetics, imaging, and clinical outcomes.

A central challenge in establishing CGIC pathways is the presence of unmeasured or poorly controlled confounders (Vandenbroucke, 2004). Mendelian Randomization (MR) offers a powerful approach to infer causal effects by leveraging genetic variants as instrumental variables (IVs), under the assumption that these variants affect the outcome only through the exposure of interest (Lawlor et al., 2008; Burgess et al., 2017; Sanderson et al., 2022). However, applying MR in high-dimensional genetic settings is complex. Genetic variables can play diverse roles—some serve as valid instruments, others act as confounders, precision covariates, or irrelevant noise. Moreover, the number of genetic variants often far exceeds the sample size, posing significant statistical and computational challenges.

Aligned with the principles of MR, we leverage genetic variants as potential IVs to investigate causal relationships between functional exposures and clinical outcomes. However, unique methodological challenges arise in this context due to the infinite-dimensional

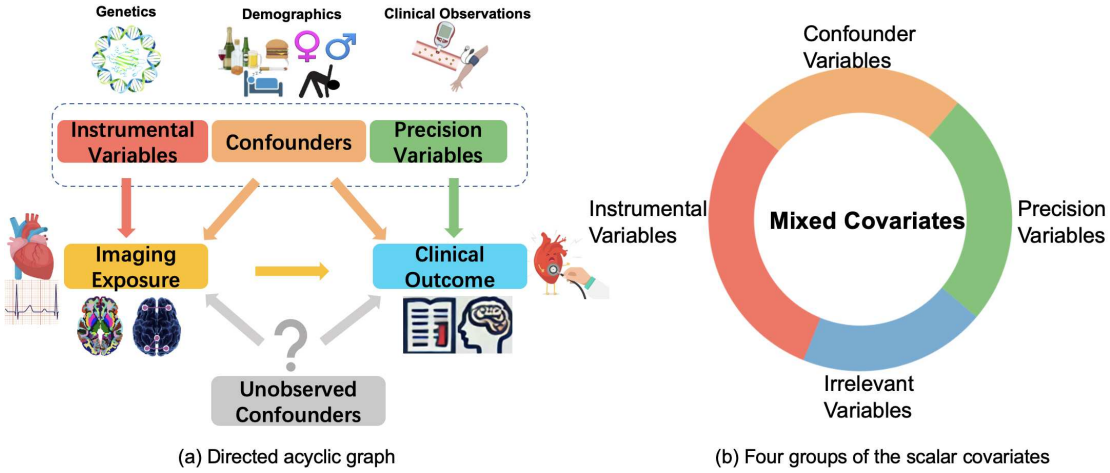


Figure 1: (a) Directed acyclic graph showing the causal genetic-imaging-clinical (CGIC) pathway that links from genetic factors to organ imaging measures to clinical outcomes confounded with environmental factors (e.g., lifestyle factors) and possible unobserved confounders. (b) Four groups of mixed covariates.

nature of functional exposures (e.g., brain imaging data), the high-dimensional and mixed roles of genetic variants, and the confounding influence of environmental and lifestyle factors on both exposures and outcomes. These complexities call for advanced statistical frameworks capable of rigorously modeling the CGIC pathway.

To enhance the robustness and interpretability of causal inference in this setting, we propose the Functional Linear Structural Equation Model (FLSEM). This model consists of two interconnected components: (i) a structural equation linking a scalar outcome to an endogenous functional exposure and scalar covariates; and (ii) an exposure model describing the functional predictor in terms of scalar instrumental variables.

Our main contributions are as follows:

(C1) We propose a three-step procedure for selecting the desired instruments and important control variables using L_0 penalty. First, we identify the relevant variables using the functional on scalar model under the reproducing kernel Hilbert space (RKHS) framework

using the L_0 penalty. Second, we replace the treatment variable with its post-adaptive predicted value and select useful controls. Third, we use the selected controls and the predicted treatment variable to obtain the treatment effect estimator following the partial functional linear model.

(C2) Different from previous studies that use the functional instrumental variables, we establish the identifiable conditions for the FLSEM, where both the instrumental covariates and useful controls are scalar. To the best of our knowledge, this is the first identifiable condition for the functional exposure model with a mixed set of scalar instruments.

(C3) We propose the Functional Group Support Detection and Root Finding (FGSDAR) algorithm to select relevant instrumental covariates for the functional exposure.

(C4) Theoretically, we establish the selection consistency of the true instruments and control, characterize the estimation error of both functional and scalar estimates, and propose a test statistic to test the nullity of the functional coefficient.

(C5) We conduct extensive simulation studies and analyze a real dataset from UK Biobank to demonstrate the finite sample performance of the proposed methods.

1.1 Related Work

Endogeneity in functional data has attracted growing attention, yet most econometric solutions still hinge on Tikhonov regularization for ill-posed inverse problems. A seminal example is Florens and Van Bellegem (2015), which establishes IV estimation for functional linear models, convergence rates, and a notion of “instrumental strength.” Subsequent work includes spline-based two-step estimators with measurement error (Tekwe et al., 2019), comparable two-step procedures with nullity tests (Jadhav et al., 2022), and fully Bayesian error correction (Zoh et al., 2022). Shifting to scalar instruments, Babii (2022) ex-

tend Florens et al.’s framework. Additional advances feature a GMM estimator for serially correlated predictors (Chen et al., 2022), an exogeneity test with asymptotic guarantees (Dorn et al., 2022), FPCA-based IV methods (Seong and Seo, 2022), and Bayesian mediation models for spatial imaging data that exploit latent-confounder structure (Xu and Kang, 2023; Xu et al., 2024). Yet none of these methods tackles the high-dimensional, mixed sets of scalar instruments and controls typical of modern genetics and neuroimaging studies. Our work closes this gap.

Our work advances function-on-scalar regression with high-dimensional scalar covariates—a setting where most methods first expand each functional coefficient in a fixed basis and then impose group penalties to achieve sparsity. Representative examples include group MCP (Chen et al., 2016) and group LASSO (Barber et al., 2017). Robust variants handle outliers via exponential-squared loss plus group SCAD (Cai et al., 2022), or by combining least-squares loss with an adaptive LASSO (Fan and Reimherr, 2017). Other directions promote simultaneous smoothness and selection through RKHS-based penalties (Parodi and Reimherr, 2018) or a smoothing elastic net (Mirshani and Reimherr, 2021). Related matrix-response work employs the trace norm for selection (Kong et al., 2019). Departing from these LASSO-type frameworks, we adopt an L_0 —penalty in the exposure model, which enforces exact sparsity without the shrinkage bias inherent to convex penalties. More importantly, whereas prior studies focus on predictive function-on-scalar models, our goal is causal: we estimate the effect of an endogenous functional exposure on a scalar outcome. To do so, we embed the L_0 —based selection within a functional-on-scalar exposure model that explicitly corrects for endogeneity, thereby extending the existing literature to high-dimensional causal inference with functional data.

The remainder of the paper is organized as follows. Section 2 introduces the FLSEM and

its identifiability conditions. Section 3 outlines the estimation procedure and proposes a test statistic to test the nullity of the functional coefficient. Section 4 establishes the consistency and convergence rates of our estimators and the null-limit theorem. Section 5 assesses the finite-sample performance via simulations. Section 6 applies the proposed methods to UK Biobank data. Proofs and additional results are included in the supplementary materials.

2 Identifiability Conditions for FLSEM

In this section, we begin by discussing the identifiability of general exposure models, laying the groundwork for examining the specific identifiability conditions of our proposed FLSEM. We consider the dataset $\{X_i, \mathbf{Z}_i, Y_i\}_{i=1}^n$, where for each sample i , $X_i = (X_{i\ell}) \in \mathbb{R}^p$ represents the scalar covariates, $\mathbf{Z}_i \in L^2(\mathcal{T})$ denotes the functional exposure, and Y_i is the corresponding response. The outcome and exposure processes are, respectively, given by

$$Y_i = \sum_{\ell=1}^p X_{i\ell} \beta_\ell + \int_{\mathcal{T}} \mathbf{Z}_i(t) \mathbf{B}(t) dt + \epsilon_i \quad \text{and} \quad \mathbf{Z}_i(t) = \sum_{\ell=1}^p f_\ell(X_{i\ell}, t) + \mathbf{E}_i(t), \quad (1)$$

where β_ℓ captures the effect of the ℓ -th scalar covariate $X_{i\ell}$ on the response Y_i , $\mathbf{B}(t)$ quantifies the impact of the functional exposure \mathbf{Z}_i on Y_i , and $f_\ell(X_{i\ell}, t)$ is a nonparametric function describing how the ℓ -th covariate influences the functional exposure \mathbf{Z}_i . Moreover, ϵ_i represents the random error in the outcome model and $\mathbf{E}_i(t)$, a random process with mean zero, accounts for additional variability in the functional exposure.

A critical aspect of these models in (1) is the potential correlation between $\mathbf{E}_i(t)$ and ϵ_i , introducing endogeneity. To address this, we set the following assumptions: (i) $E(\epsilon_i | X_i) = 0$ and $E\{\mathbf{E}_i(t) | X_i\} = 0$, ensuring that the error terms are conditionally zero mean independent of the covariates. (ii) $E(\epsilon_i | \mathbf{Z}_i) \neq 0$ and $E\{\epsilon_i \mathbf{E}_i(t)\} \neq 0$, reflecting the influence of unobserved confounders. These model specifications and assumptions form the basis for our subsequent analysis, where we focus on the identifiability challenges posed by endogeneity

and develop methods to address them within the FLSEM framework.

Following Yu et al. (2022), we organize all covariates into four distinct groups in $\mathcal{A} = \{1, \dots, p\}$ (Figure 1 (b)). Let $\mathcal{C} = \{\ell \in \mathcal{A} \mid \beta_\ell \neq 0 \text{ and } f_\ell \neq 0\}$ denote the indices of confounders, which are associated with both the outcome and the exposure. The set $\mathcal{P} = \{\ell \in \mathcal{A} \mid \beta_\ell \neq 0 \text{ and } f_\ell = 0\}$ includes precision variables that affect the outcome but not the exposure. The set $\mathcal{I} = \{\ell \in \mathcal{A} \mid \beta_\ell = 0 \text{ and } f_\ell \neq 0\}$ represents IVs that influence the exposure but not the outcome. Lastly, $\mathcal{S} = \{\ell \in \mathcal{A} \mid \beta_\ell = 0 \text{ and } f_\ell = 0\}$ corresponds to irrelevant variables with no association to either. According to Guo et al. (2018), \mathcal{I} consists of valid instruments, whereas \mathcal{C} contains invalid instruments due to their dual association with both outcome and exposure.

In our outcome model, $\mathbf{Z}_i(t)$ may be correlated with the error term ϵ_i , violating the exogeneity assumption in classical partial functional linear regression models (Kong et al., 2016; Yu et al., 2022). Here, the coefficient $\mathbf{B}(t)$ captures the causal effect of changes in $\mathbf{Z}_i(t)$ on Y_i , rather than mere association. Standard approaches (Kong et al., 2016; Li and Zhu, 2020) may yield biased estimates by ignoring potential endogeneity in $\mathbf{Z}_i(t)$. To address this, we incorporate the exposure model and IVs derived from X_i , establishing identifiability of $\mathbf{B}(t)$ and enabling valid causal estimation. This strategy clarifies the $\mathbf{Z}_i(t)$ – Y relationship and strengthens the validity of our causal inferences.

2.1 Identifiability Condition for General f

The identifiability of parameters with scalar exposures has been well studied. For example, Kang et al. (2016) propose the “50% rule,” requiring a majority of instruments to be valid, while Guo et al. (2018) relax this to a “plurality rule” for broader applicability. Building on these insights, we extend identifiability conditions to the more complex setting

of functional exposures. The infinite-dimensional nature of functional treatments poses unique challenges, particularly when instruments may be invalid. To our knowledge, this is the first study to address identifiability under such conditions.

Following model (1), let $f(X_i, t) = \sum_{\ell=1}^p f_{\ell}(X_{i\ell}, t)$, we have the moment condition that

$$g(X_i) = E(Y_i|X_i) = X_i^{\top} \beta + \int_{\mathcal{T}} f(X_i, t) \mathbf{B}(t) dt, \quad (2)$$

leading to $M_X g(X_i) = \int_{\mathcal{T}} M_X f(X_i, t) \mathbf{B}(t) dt$, where M_X represents the orthogonal space of the linear space spanned by X . Let $\mathcal{K}\mathbf{B}(t) = \int_{\mathcal{T}} E\{M_X f(X_i, s) M_X f(X_i, t)\} \mathbf{B}(s) ds$. Using the inverse of linear integral equations (Hsing and Eubank, 2015), we present a straightforward and intuitive condition for identifying $\mathbf{B}(s)$.

Proposition 1. *Consider the reduced form (2), if the operator \mathcal{K} is injective, and the null space of the operator \mathcal{K} only contains 0 such that $\mathcal{N}(\mathcal{K}) = \{0\}$, then $\mathbf{B}(t)$ is identifiable.*

Proposition 1 follows directly from Theorem 3.5.1 of Hsing and Eubank (2015). Specifically, if there exists $\mathbf{B}_1(s)$ and $\mathbf{B}_2(s)$ satisfying $\mathcal{K}\mathbf{B}_1(s) = \mathcal{K}\mathbf{B}_2(s)$, or equivalently $\mathcal{K}(\mathbf{B}_1(s) - \mathbf{B}_2(s)) = 0$, it directly implies that $\mathbf{B}_1(s) = \mathbf{B}_2(s)$. This proposition extends the relevance rank condition (Liang et al., 2022) commonly employed in linear IV models with scalar exposures to functional exposure. Notably, it differs from prior studies such as Florens and Van Bellegem (2015) and Babii (2022), where IVs are either provided or constructed based on an injective operator derived from the logistic cumulative distribution function. Instead, we consider infinite-dimensional IVs $f(X, t)$. Furthermore, Proposition 1 considers the linear effect of X on Y , and nonlinear effect of X on \mathbf{Z} , which separates the effects of the instruments and the confounders.

For the integral operator \mathcal{K} , the kernel $K(s, t) = E\{f(X, s)f(X, t)\}$ plays a fundamental role. Mercer's theorem provides the spectral decomposition $K(s, t) = \sum_{k=1}^{\infty} \lambda_k \varphi_k(s) \varphi_k(t)$,

where $\{\varphi_k(\cdot), \lambda_k \geq 0\}_{k \geq 1}$ forms an orthonormal basis in $L^2(\mathcal{T})$. Any $\mathbf{B}(t) \in L^2(\mathcal{T})$ can be expressed as $\mathbf{B}(t) = \sum_{k=1}^{\infty} b_k \varphi_k(t)$ and $\mathcal{K}\mathbf{B}(s) = \sum_k \lambda_k b_k \varphi_k(s)$. The condition in Proposition 1 requires that $\lambda_k > 0$ for all $k \geq 1$. Consequently, if $\mathcal{K}\mathbf{B}(s) = 0$, it implies $b_k = 0$ for all k and then $\mathbf{B}(s) = 0$.

We present several examples of kernel functions that satisfy our assumptions. The Ornstein-Uhlenbeck kernel $K(s, t) = \exp(-|t-s|)$ and the Brownian motion kernel $K(s, t) = \min(s, t)$ both meet the required conditions. In addition, a range of reproducing kernels—such as polynomial splines, periodic splines, thin-plate splines, exponential splines, and logistic splines (Wang, 2011)—are injective mappings. These kernels also exhibit appropriate eigenvalue decay behaviors: for polynomial decay kernels, $\lambda_k \asymp k^{-2r}$, while for exponential decay kernels, $\lambda_k \asymp \exp(-\alpha k^r)$, both satisfying our theoretical assumptions.

2.2 Identifiability Condition for linear f

We investigate the linear case when f is linear in X . In this case, model (1) simplifies to

$$Y_i = \sum_{\ell=1}^p X_{i\ell} \beta_\ell + \int_{\mathcal{T}} \mathbf{Z}_i(t) \mathbf{B}(t) dt + \epsilon_i \quad \text{and} \quad \mathbf{Z}_i(t) = \sum_{\ell=1}^p X_{i\ell} C_\ell(t) + \mathbf{E}_i(t). \quad (3)$$

Although there is one exposure, identifying the causal effect $\mathbf{B}(t)$ remains challenging due to a limited number of instruments. For simplicity, we consider valid IVs such that $Y_i = \int_{\mathcal{T}} \mathbf{Z}_i(t) \mathbf{B}(t) dt + \epsilon_i$ and $\mathbf{Z}_i(t) = X_i^\top \mathbf{C}(t) + \mathbf{E}_i(t) = \tilde{\mathbf{Z}}_i(t) + \mathbf{E}_i(t)$. Projecting $\mathbf{Z}(t)$ onto the space of X leads to $\tilde{\mathbf{Z}} = X^\top \mathbf{C}(t)$. It follows that

$$E[Y|X] = X^\top \int_{\mathcal{T}} C(t) \mathbf{B}(t) dt + 0 = \int_{\mathcal{T}} \tilde{\mathbf{Z}}(t) \mathbf{B}(t) dt.$$

Here, the linear operator takes the form $\mathcal{K}\mathbf{B}(t) = \int_{\mathcal{T}} E\{\tilde{\mathbf{Z}}(s) \tilde{\mathbf{Z}}(t)\} \mathbf{B}(s) dt$. A naive identifiable condition of $\mathbf{B}(s)$ hinges on $\mathcal{N}(\mathcal{K}) = \{0\}$. However, $\tilde{\mathbf{Z}}(t)$ typically contains less information compared to $\mathbf{Z}(t)$, making it challenging to satisfy the injectivity condition.

Specifically, $\mathcal{K}\mathbf{B}(s)$ has the form

$$\mathcal{K}\mathbf{B}(s) = \int_{\mathcal{T}} \mathbf{C}(t)^\top E(XX^\top) \mathbf{C}(s) \mathbf{B}(t) dt = \int_{\mathcal{T}} \mathbf{C}(t)^\top E(XX^\top) \mathbf{B}(t) dt \mathbf{C}(s).$$

Thus, the null space of \mathcal{K} is $\mathcal{N}(\mathcal{K}) = \{\mathbf{B} : \int_{\mathcal{T}} \mathbf{C}(t)^\top E(XX^\top) \mathbf{B}(t) dt = 0\}$. Then $\mathbf{B}(t)$ is not identifiable for $\mathbf{B} \in \mathcal{N}(\mathcal{K})$ because the solutions to the functional normal equation are not unique. To address this issue, methods like the Moore-Penrose generalized inverse (see e.g., Definition 3.5.7 in Hsing and Eubank, 2015) and regularization techniques such as Tikhonov regularization are popular (Engl et al., 1996).

While these methods guarantee a unique solution, they recover only the component of $\mathbf{B}(t)$ that lies in the subspace $\mathcal{N}(\mathcal{K})^\perp$, the orthogonal complement of the null space of \mathcal{K} . The dimension of $\mathcal{N}(\mathcal{K})$ is inversely related to the number of valid instruments: as the number of valid instruments increases, the null space shrinks, improving the identifiability of $\mathbf{B}(t)$. This highlights how richer instrumental information enhances the estimation of the leading components of the causal effect $\mathbf{B}(t)$ under appropriate conditions.

Before detailing the identifiable conditions, we first establish some mild assumptions regarding the functional forms of $\mathbf{B}(t)$ and $\mathbf{C}(t)$. Assume that $\mathbf{B}(t) = \sum_{k=1}^{\infty} b_k \varphi_k(t)$ and $\mathbf{C}(t) = \sum_{k=1}^{\infty} \mathbf{c}_k \varphi_k(t)$, where $\{\varphi_k(t)\}$ represents an orthogonal basis. Model (3) implies

$$E[X_i \{Y_i - X_i^\top \beta - \int_{\mathcal{T}} \mathbf{Z}_i(t) \mathbf{B}(t) dt\}] = 0 \quad \text{and} \quad E[X_i \{\mathbf{Z}_i(t) - X_i^\top \mathbf{C}(t)\}] = 0.$$

Letting $\Gamma^* = (\Gamma_{\ell}^*) = E(X_i X_i^\top)^{-1} E(X_i Y_i)$, we have that

$$\Gamma^* = \beta + \int_{\mathcal{T}} \mathbf{C}(t) \mathbf{B}(t) dt = \beta + \sum_{k=1}^{\infty} b_k \mathbf{c}_k \approx \beta + \sum_{k=1}^R b_k \mathbf{c}_k, \quad (4)$$

where R is a positive integer. If $\int_{\mathcal{T}} \mathbf{C}(t) \mathbf{B}(t) dt$ can be well approximated by $\sum_{k=1}^R b_k \mathbf{c}_k$ (He et al., 2000; Cardot et al., 2003; Shin, 2009), then the leading coefficients $\{b_k\}_{k=1}^R$ can be identified under some conditions. If the l -th covariate X_l is a valid instrument, then $\beta_l = 0$.

The estimates of Γ^* and $\{\mathbf{c}_k\}$ can be obtained by examining the relationship between the outcome and the potential instruments, and that between the exposure and the potential instruments. Theorem 1 below gives the identification condition at the presence of possible invalid instruments.

Recall that \mathcal{I} denotes the set of valid instruments, while \mathcal{C} represents the set of invalid instruments. Let the total number of instruments be $L = p_{\mathcal{I}} + p_{\mathcal{C}}$, where $p_{\mathcal{I}} = |\mathcal{I}|$ and $p_{\mathcal{C}} = |\mathcal{C}|$ denote the number of valid and invalid instruments, respectively. We impose a mild assumption that the number of invalid instruments is bounded above: $p_{\mathcal{C}} < U$ for some $U \leq L$. Importantly, this condition does not require knowledge of the exact identities or number of invalid instruments. Under this setup, the following theorem establishes that a meaningful coefficient can still be identified.

Theorem 1. *Suppose that $\int_{\mathcal{T}} \mathbf{C}(t) \mathbf{B}(t) dt$ can be approximated by $\sum_{k=1}^R b_k \mathbf{c}_k$ for some vectors \mathbf{c}_k 's such that $\int_{\mathcal{T}} \mathbf{C}(t) \mathbf{B}(t) dt = \sum_{k=1}^R b_k \mathbf{c}_k + o(R^{-2r})$ for some $r \geq 1$. Consider all sets $S_m \subseteq \{1, \dots, L\}$ of size $|S_m| = L - U + 1 > R$ for all $m = 1, \dots, M$ with the property that there exists a unique $\{b_k^{(m)}\}_{k=1}^R$ satisfying $\sum_{k=1}^R b_k^{(m)} \mathbf{c}_{\ell k} = \Gamma_{\ell}^*$ for $\ell \in S_m$. There is a unique solution β and $\{b_k\}_{k=1}^R$ to (4) if and only if the subspace-restriction condition holds, that is $b_k^{(m)} = b_k^{(m')}$ for all $m, m' \in \{1, \dots, M\}$ and $k = 1, \dots, R$.*

Theorem 1 shows that while the full recovery of $\mathbf{B}(t)$ may not be possible in the presence of invalid instruments, its leading components can be consistently identified under suitable subspace restrictions. This extends the identifiability framework for a single endogenous variable (Kang et al., 2016; Guo et al., 2018) to the more complex and less explored setting with K endogenous variables. Specifically, Theorem 1 states that $\{b_k\}_{k=1}^R$ is identifiable if no two distinct instrument subsets of size at least $L - U + 1$ yield the same coefficient estimates on any common set of R instruments while producing inconsistent results when

combined. This condition ensures that valid instruments provide sufficient identifying power and that no subset of invalid instruments can generate indistinguishable projections.

We illustrate Theorem 1 with two examples. (i) Suppose there are five relevant instruments with $L = 5$, $R = 2$, $U = 3$, and $\Gamma^* = (2, 3, 3, 8, 5)^T$. Let $(c_{11}, \dots, c_{51}) = (1, 1, 2, 1, 2)$ and $(c_{12}, \dots, c_{52}) = (1, 2, 1, 1, 3)$. According to Theorem 1, we have $M = 2$ and two instrument subsets $S_1 = \{1, 2, 3\}$ and $S_2 = \{2, 3, 5\}$. One can verify that $b_1^{(1)} = 1$ and $b_2^{(1)} = 1$ satisfy $\sum_{k=1}^2 b_k^{(1)} c_{\ell k} = \Gamma_\ell^*$ for all $\ell \in S_1$, while $b_1^{(2)} = 1$ and $b_2^{(2)} = 1$ hold similarly for S_2 . As a result, there is a unique solution for β and $\{b_k\}_{k=1}^R$ with $p_I = 4$ and $p_C = 1$. (ii) Consider a different setting with $R = 2$, $U = 4$, $\Gamma^* = (2, 3, 6, 8, 10)^T$, $(c_{11}, \dots, c_{51}) = (1, 1, 1, 2, 2)$, and $(c_{12}, \dots, c_{52}) = (1, 2, 3, 2, 3)$. In this case, $M = 2$ and the subsets are $S_1 = \{1, 2\}$ and $S_2 = \{4, 5\}$ with $b_1^{(1)} = 1$, $b_2^{(1)} = 1$, $b_1^{(2)} = 2$, and $b_2^{(2)} = 2$. However, these values fail to satisfy the consistency requirement, so there is no unique solution for the system. We cannot distinguish between valid and invalid instruments.

While it may be difficult to check the condition in Theorem 1 in general, the following corollary presents a sufficient condition that is easy to check in practice.

Corollary 1. *Suppose the conditions in Theorem 1 hold, if the maximal number of invalid instruments $U \leq (L - R + 1)/2$, there is a unique solution to (4).*

Corollary 1 provides a computationally feasible criterion for verifying the identifiability conditions in Theorem 1. The key requirement is that any set of R valid instruments must yield a unique solution for the coefficient vector $\{b_k\}_{k=1}^R$, which amounts to uniquely solving the R equations $\sum_{k=1}^R b_k^{(m)} c_{lk} = \Gamma_l^*$, $l = 1, \dots, R$. Rather than exhaustively checking all subsets of instruments, the corollary simplifies verification by requiring that the number of invalid instruments be strictly less than $(L - R + 1)/2$. This generalizes the classical majority rule of Kang et al. (2016) to the more complex setting involving endogenous

functional variables. Notably, when $R = 1$, the result reduces to the standard majority rule for scalar endogenous variable.

In biomedical research, many genetic variants identified through Genome-Wide Association Studies (GWAS) are relevant to downstream analyses. While researchers may have a rough estimate of the maximum number of invalid instruments U , the precise identities of these instruments are typically unknown. The effects of an endogenous functional exposure can still be identified, as long as the number of invalid instruments is less than $(L - R + 1)/2$.

3 Estimation

We estimate the coefficient $\mathbf{B}(t)$ in (3) using a three-step strategy, starting with a fast screening procedure designed for the $p \gg n$ regime. In this initial step, we reduce the covariate set by applying two complementary filters: (i) sure independence screening on (Y_i, X_i) (Fan and Lv, 2008), and (ii) distance-correlation screening on the functional pair $(Z_i(t), X_i)$ (Li et al., 2024). Taking the union of these selected predictors produces a joint screening set that retains the most informative variables while ensuring that subsequent estimation remains both statistically sound and computationally feasible.

Second, we estimate the fitted value of $\mathbf{Z}_i(t)$ by fitting the model in (1) with separate controls for smoothness and sparsity. Building on Mirshani and Reimherr (2021), we replace their elastic-net sparsity penalty with an L_0 constraint, yielding the first function-on-scalar regression with exact sparsity. We solve $\widehat{\mathbf{C}}$ by minimizing

$$L_\lambda(\mathbf{C}) = \frac{1}{2n} \|\mathbf{Z} - \mathbf{X}^\top \mathbf{C}(t)\|_2^2 + \frac{\lambda_K}{2} \sum_{\ell=1}^p \|C_\ell\|_K^2 + \lambda_0 \|\mathbf{C}\|_0 \quad (5)$$

over $\mathbf{C}(t) \in \mathcal{H}(K)$, where $\mathbf{C}(t) = (C_1(t), \dots, C_p(t))^\top$, \mathbf{X} stacks the n observations where the i -th row is X_i^\top and $\mathbf{Z} = (\mathbf{Z}_1(t_1), \dots, \mathbf{Z}_1(t_m), \dots, \mathbf{Z}_n(t_1), \dots, \mathbf{Z}_n(t_m))$. By the Repre-

senter Theorem (Wahba, 1990), each estimator $\widehat{C}_\ell(t)$ satisfies

$$\widehat{C}_\ell(t) = C_\ell^\top K(t), \quad C_\ell \in \mathbb{R}^m, \quad K(t) = (K(t, t_1), \dots, K(t, t_m))^\top.$$

Smoothness is enforced by the RKHS norm $\|C_\ell\|_{\mathcal{K}} = \sqrt{C_\ell^\top \Sigma C_\ell}$, where $\Sigma = (\Sigma_{ii'}) = (K(t_i, t_{i'}))$, while the L_0 term selects at most J nonzero functions. This finite-dimensional formulation has been well studied in the RKHS literature (Zhang et al., 2022). Under the condition that $p \ll n$, the functional estimates have the following form with $\check{\mathbf{X}} = \mathbf{X} \otimes \Sigma$,

$$\widehat{\mathbf{C}} = (\widehat{C}_1^\top, \dots, \widehat{C}_p^\top)^\top = (\check{\mathbf{X}}^\top \check{\mathbf{X}} + nm\lambda_K \Sigma)^{-1} \check{\mathbf{X}}^\top \mathbf{Z}.$$

Building on the finite-dimensional representation of the functional coefficients, we propose the Functional Group Support Detection and Root Finding (FGSDAR) algorithm (Algorithm 1) to efficiently optimize the loss function in (5). FGSDAR extends the support detection and root-finding framework of Huang et al. (2018) to the functional response setting. The algorithm employs a blockwise coordinate descent strategy, iteratively updating the active set (indices with nonzero coefficients) and the inactive set (zero coefficients). Estimation is performed only on the active set, thereby reducing model complexity and improving computational efficiency. For any index set $A \subseteq \{1, 2, \dots, p\}$ with size $|A|$, let $\mathbf{C}_A = \{\mathbf{C}_\ell(t) : \ell \in A\}$, and similarly define $\check{\mathbf{X}}_A$. Let $\mathbf{C}|_A$ denote the vector where the ℓ -th component is given by $(\mathbf{C}|_A)_\ell = \mathbf{C}_\ell(t) \mathbb{1}(\ell \in A)$, with $\mathbb{1}(\cdot)$ denoting the indicator function. Let $\|\mathbf{C}\|_{J,\infty}$ represent the J -th largest L_2 -norm among the coefficient functions. The validity of FGSDAR in identifying a local minimizer is established in Lemma ?? of the supplementary materials.

Third, we write the outcome generating model as

$$Y_i = \sum_{\ell=1}^p X_{i\ell} \beta_\ell + \int_{\mathcal{T}} E\{\mathbf{Z}_i(t)|X_i\} \mathbf{B}(t) dt + \nu_i = \sum_{\ell=1}^p X_{i\ell} \beta_\ell + \int_{\mathcal{T}} \widehat{\mathbf{Z}}_i(t) \mathbf{B}(t) dt + \hat{\nu}_i, \quad (6)$$

Algorithm 1 Functional group support detection and root finding (FGSDAR)

Input: An initial \mathbf{C}^0 and the group sparsity level J ; set $k = 0$.

- 1: Calculate $d^0 = \check{\mathbf{X}}^\top (\mathbf{Z} - \tilde{\mathbf{X}}\mathbf{C}^0) - nm\lambda_K\Sigma\mathbf{C}^0$ for a given smoothness parameter λ_K ;
- 2: **for** $k = 0, 1, 2, \dots$ **do**
- 3: $A_R^k = \{\ell : \|\mathbf{C}_\ell^k + d_\ell^k\|^2 \geq \|\mathbf{C}^k + d^k\|_{J,\infty}^2\}$, $I_R^k = (A_R^k)^c$;
- 4: $\mathbf{C}_{A_R^k}^{k+1} = (\check{\mathbf{X}}_{A_R^k}^\top \check{\mathbf{X}}_{A_R^k} + nm\lambda_K\Sigma)^{-1} \check{\mathbf{X}}_{A_R^k}^\top \mathbf{Z}$;
- 5: $d_{I_R^k}^{k+1} = \check{\mathbf{X}}_{I_R^k}^\top (\mathbf{Z}_R - \check{\mathbf{X}}_{A_R^k} \mathbf{C}_{A_R^k}^k) - nm\lambda_K\Sigma\mathbf{C}_{I_R^k}^k$;
- 6: **if** $A_R^{k+1} = A_R^k$ **then** Stop.
- 7: **else** $k = k + 1$;
- 8: **end if**
- 9: **end for**

- 10: Select λ_K by minimizing the generalized cross-validation (GCV) criterion;

Output: $\widehat{\mathbf{C}}$, A_R^k , and I_R^k .

where $\nu_i = Y_i - E(Y_i|X_i) = \int_{\mathcal{T}} [\mathbf{Z}_i(t) - E\{\mathbf{Z}_i(t)|X_i\}] \mathbf{B}(t) dt + \epsilon_i$ satisfies $E[\nu_i E\{\mathbf{Z}_i(t)|X_i\}] =$

0. Assume that $\mathbf{B}(t)$ resides in an RKHS \mathcal{H} . Consider the minimization problem

$$\min_{\beta \in \mathbb{R}^p, \mathbf{B} \in \mathcal{H}} \left[\frac{1}{2n} \sum_{i=1}^n \left\{ Y_i - \left(\sum_{l=1}^p X_{il} \beta_l + \int_{\mathcal{T}} \widehat{\mathbf{Z}}_i(t) \mathbf{B}(t) dt \right) \right\}^2 + \tau \|\beta\|_0 + \frac{\lambda}{2} \|\mathbf{B}\|_{\mathcal{K}}^2 \right], \quad (7)$$

where τ and λ are tuning parameters. Replacing $\mathbf{Z}_i(t)$ with $\widehat{\mathbf{Z}}_i(t)$ partials out the effect of $\widehat{\mathbf{Z}}_i(t)$ when selecting important variables for the outcome. The algorithm proposed in Li et al. (2024) is adopted to solve (7), deriving $\widehat{\mathcal{P}} \cup \widehat{\mathcal{C}} = \{\ell : |\widehat{\beta}_\ell| > 0\}$ and $\widehat{\mathbf{B}}(t)$.

The computational cost of solving problem (5) grows prohibitively large when the sample size n or the number of grid points m increases. For example, in the UK Biobank imaging cohort, n can reach 100,000, and a single hippocampus image with 100×150 resolution yields $m = 15,000$ grid points. Evaluating (5) over all samples and grid locations is therefore infeasible using standard optimization routines.

To address this challenge, we propose a region-based estimation algorithm tailored for large-scale problems. To handle the large sample size, we adopt a divide-and-conquer strategy (Zhang et al., 2015; Lian and Fan, 2018; Hong et al., 2022), which partitions the dataset into \tilde{n} subsets of equal size, each containing n/\tilde{n} subsamples. This allows us to process smaller, tractable subproblems independently. In parallel, to accommodate the high spatial resolution of the imaging data, we introduce a sliding-window approach inspired by techniques in genetic data analysis (Hudson and Kaplan, 1988). Specifically, the window moves across the imaging grid to generate overlapping subregions $\{\mathcal{T}_1, \dots, \mathcal{T}_m\}$ that together cover the entire imaging domain $\mathcal{T} = \bigcup_{k=1}^m \mathcal{T}_k$. This dual strategy—dividing subjects and sliding over functional domains—yields significant computational savings and enables scalable analysis of large, high-dimensional imaging datasets.

After partitioning the data into \tilde{n} subsamples and regions $\{\mathcal{T}_k\}$, we apply the following distributed, region-based estimation: (i) **Local Estimation.** For each subsample $\zeta = 1, \dots, \tilde{n}$ and region \mathcal{T}_k , solve (5) to obtain $\hat{\mathbf{C}}_\ell^{\zeta k}(t)$, $\ell = 1, \dots, p$, $t \in \mathcal{D}_k$. (ii) **Regional Aggregation.** Within each region \mathcal{T}_k , average across subsamples: $\bar{\mathbf{C}}_\ell^k(t) = \tilde{n}^{-1} \sum_{\zeta=1}^{\tilde{n}} \hat{\mathbf{C}}_\ell^{\zeta k}(t)$. (iii) **Function Reconstruction.** For each subject i and $t \in \mathcal{T}_k$, reconstruct $\hat{\mathbf{Z}}_i(t) = \sum_{\ell=1}^p X_{i\ell} \bar{\mathbf{C}}_\ell^k(t)$. (iv) **Overlap Synthesis.** Since regions overlap, compute the final estimate at each grid point by averaging all predictions covering that point.

In addition to estimating the true $\mathbf{B}^*(t)$, we also test whether this effect is identically zero. Concretely, we consider the hypotheses $H_0 : \mathbf{B}^*(t) = 0 \quad \forall t$ v.s. $H_1 : \exists t \text{ s.t. } \mathbf{B}^*(t) \neq 0$. Recall that by construction, there exists $\mathbf{F}^*(t) \in L^2(\mathcal{T})$ satisfying $\mathbf{B}^*(t) = K^{1/2} \mathbf{F}^*(t)$. Because $K^{1/2}$ is invertible on its support, testing $\mathbf{B}^*(t) \equiv 0$ is equivalent to testing $H_0 : \mathbf{F}^*(t) \equiv 0 \quad \forall t$, which we use as the basis for our inferential procedure.

Similar to Cai and Yuan (2012), the solution to (7) admits the closed-form

$$\widehat{\mathbf{F}}(t) = n^{-1} (R_n + \lambda I)^{-1} (K^{1/2} \widehat{\mathbf{Z}}(t))^{\top} \mathcal{M}_{\widehat{A}} Y, \quad (8)$$

where $R_n = n^{-1} K^{1/2} \widehat{\mathbf{Z}}(s)^{\top} \mathcal{M}_{\widehat{A}} \widehat{\mathbf{Z}}(t) K^{1/2}$ is the empirical analogue of the operator $R = n^{-1} K^{1/2} E\{\widetilde{\mathbf{Z}}(s)^{\top} \mathcal{M}_{A^*} \widetilde{\mathbf{Z}}(t)\} K^{1/2}$, with $\widetilde{\mathbf{Z}} = X^{\top} \mathbf{C}(t)$, and I denotes the identity operator.

The estimated active set of precision and confounder variables from (6) is denoted as $\widehat{A} = \widehat{\mathcal{P} \cup \mathcal{C}} = \{\ell : |\widehat{\beta}_{\ell}| > 0\}$, while A^* represents the true useful control set. For any subset A , \mathbf{X}_A consists of the columns $\{\ell : \ell \in A\}$ from \mathbf{X} . The operator $\mathcal{M}_A = I - \mathbf{X}_A (\mathbf{X}_A^{\top} \mathbf{X}_A)^{-1} \mathbf{X}_A^{\top}$ projects out the influence of scalar covariates on the outcome. To test $H_0: \mathbf{F}^*(t) \equiv 0$, we examine the squared norm of $(R_n + \lambda I) \widehat{\mathbf{F}}(t)$. This yields the test statistic

$$S_n = n \left\| (R_n + \lambda I) \widehat{\mathbf{F}}(t) \right\|_2^2 / \widehat{\sigma}^2 = Y^{\top} \mathcal{M}_{\widehat{A}} \int_{\mathcal{T}} \int_{\mathcal{T}} \widehat{\mathbf{Z}}(s)^{\top} K(s, t) \widehat{\mathbf{Z}}(t) ds dt \mathcal{M}_{\widehat{A}} Y / (n \widehat{\sigma}^2),$$

where $\widehat{\sigma}^2$ is the estimated variance of the outcome model residuals.

4 Theoretical Properties

We now turn to the theoretical analysis of our estimators and test statistic. Denote $\|\mathbf{C}\|_2^2 = \sum_{j=1}^p \|C_j\|_2^2 = \sum_{j=1}^p \int_{\mathcal{T}} C_j^2(t) dt$. Let $\delta^* = (\delta_1^*, \dots, \delta_p^*)^{\top} \in (L_2(\mathcal{T}))^p$ be $\delta_j^* = \arg \min_{\delta \in L^2(\mathcal{T})} E(X_j - \int_{\mathcal{T}} \mathbf{Z}(t) \delta(t) dt)^2$ for $j = 1, \dots, p$, corresponding to the projection onto the space spanned by $\{\mathbf{Z}(t)\}_{t \in \mathcal{T}}$ for each covariate X_j . Using these population projections, we form the residualized covariates $\widetilde{X}_{ij} = X_{ij} - \int_{\mathcal{T}} \mathbf{Z}_i(t) \delta_j^*(t) dt$ and $\widetilde{X}_i = (\widetilde{X}_{i1}, \dots, \widetilde{X}_{ip})^{\top}$, and stack them across subjects into $\widetilde{\mathbf{X}} = (\widetilde{X}_1^{\top}, \dots, \widetilde{X}_n^{\top})^{\top}$.

Assumption 1. *The input sparsity levels for Algorithm 1 and for (7) satisfy $J \geq \max(J_y^*, J_z^*)$, where J_y^* and J_z^* are the true sparsity levels for the scalar and imaging responses.*

Assumption 2. For the input sparsity levels J , \mathbf{X} satisfies the sparse Riese condition (Huang et al., 2018) that $\tilde{\mathbf{X}}, \mathbf{X} \sim SRC\{2J, c_-(2J), c_+(2J)\}$ for $A, B \subseteq S$, $|A| \leq J$, $|B| \leq J$, and $A \cap B = \emptyset$ and $\forall u \neq 0 \in \mathbb{R}^{|A|}$, $0 < c_-(J) \leq \|\mathbf{X}_A u\|_2^2 / (n\|u\|_2^2) < c_+(J)$ and $\theta_{J,J} \geq \|\mathbf{X}_B^\top \mathbf{X}_A u\|_2 / (n\|u\|_2)$, where $c_-(J)$ is an increasing function of J , $c_+(J)$ is a decreasing function of J , and $\theta_{J,J} = \max\{(1 - c_-(2J)), (c_+(2J) - 1)\}$ is an increasing function of J .

Assumption 3. For any function $\mathbf{B} \in \mathcal{H}$, there exists some positive constant c_1 satisfying

$$E\left\{\int_0^1 \mathbf{Z}(t) \mathbf{B}(t) dt\right\}^4 \leq c_1 \left(E\left\{\int_0^1 \mathbf{Z}(t) \mathbf{B}(t) dt\right\}^2\right)^2$$

Assumption 4. For $j = 1, \dots, p$, $\tilde{X}_{1j}, \dots, \tilde{X}_{nj}$ are independently and identically distributed with mean zero and $\sigma_x^2 = \max\{Var(\tilde{X}_{ij}^2), j = 1, \dots, p\}$ is finite.

Assumption 5. The coefficients $\delta_j^* \in \mathcal{H}$ for $j = 1, \dots, p$ and $\delta_{\max} = \max_j \|\delta_j^*\|_{\mathcal{H}} < \infty$.

Assumption 6. The random errors $\epsilon_1, \dots, \epsilon_n$ are independently and identically distributed with mean zero, variance σ^2 and sub-Gaussian tails.

Assumption 7. There exists some constant $C_K > 0$ such that $\sup_t K(t, t) \leq C_K$.

Assumption 8. The errors $E_i(t)$ are identically independent and satisfy that $E\{E_i(t)\} = 0$, $\sup_t E\{E_i(t)\}^2 < \sigma_E^2 < \infty$, and the covariance function $Cov(E_i(t), E_i(s)) = G(s, t)$ for $s, t \in [0, 1]$ satisfies $0 < c_G \leq G(s, s) \leq C_G \leq \infty$.

Assumptions 1 and 2 mirror conditions in Huang et al. (2018). In particular, Assumption 1 requires that our chosen sparsity level exceed the true model's sparsity, ensuring all nonzero coefficients can be recovered. Assumption 2 imposes restricted eigenvalue-type bounds on the diagonal blocks of both $\mathbf{X}^\top \mathbf{X} / n$ and $\tilde{\mathbf{X}}^\top \tilde{\mathbf{X}} / n$, thereby controlling multicollinearity among predictors. Assumption 3, standard in functional regression theory (e.g., Yuan and Cai (2010)), governs the fourth-moment behavior of the functional covariates. Assumption 4 then bounds the projection error of scalar covariates onto the functional

space, while Assumption 5 requires that the projection functions δ_j^* lie in the same RKHS as the true $\mathbf{B}(t)$ (see also Shin (2009); Li and Zhu (2020)). Finally, Assumption 6 is the usual sub-Gaussian noise condition (Huang et al. (2018)), Assumption 7 places regularity conditions on the RKHS kernel (Zhang et al., 2015), and Assumption 8 controls the mean and variance structure of the imaging-error process.

We begin by quantifying the approximation error for our solution sequence of $\mathbf{C}(t)$. Let $\mathbf{C}^*(t)$ denote the true functional coefficient vector, and define two true active index sets: $A_R^* = \{j : \mathbf{C}_j(t) \neq 0\}$ and $A^* = \{j : \beta_j \neq 0\}$ for the imaging and the scalar outcome.

Theorem 2. *Let J be the user-specified sparsity level in FGSDAR, and let A_R^{k+1} denote the active set estimated at iteration $k+1$. Under Assumptions 1, 2, 7, and 8, and for a contraction constant $\gamma < 1$ defined in (??) of the supplement, the following bounds hold:*

$$\|\mathbf{C}^*|_{A_R^* \setminus A_R^{k+1}}\|_2 \leq \gamma^{k+1} \|\mathbf{C}^*\|_2 + \frac{\gamma}{1-\gamma} h(J, \lambda_K), \quad \|\mathbf{C}^{k+1} - \mathbf{C}^*\|_2 \leq b_1 \gamma^k \|\mathbf{C}^*\|_2 + b_2 h(J, \lambda_K),$$

where $h(J, \lambda_K) = \max_{|A|=J} \left\| (T_{nm}^A + \lambda_K I)^{-1} \left((nm)^{-1} \sum_{i=1}^n \sum_{j=1}^m E_i(t_j) K_{t_{ij}} X_{i,A} + \lambda_K \mathbf{C}_A^* \right) \right\|_2$,

and $T_{nm}^A : \mathcal{K} \rightarrow \mathcal{K}$ is the empirical operator $T_{nm}^A f = (nm)^{-1} \sum_{i=1}^n \sum_{j=1}^m \langle X_{i,A}^\top f, K_{t_{ij}} \rangle_{\mathcal{K}} K_{t_{ij}} X_{i,A}^\top$.

The constants b_1 , and b_2 are given in (??) of the Supplement. Moreover, for any $\nu \in (0, 1/2)$, $h(J, \lambda_K) \leq \sigma_E \sqrt{J \log(p/\nu)} \sqrt{\text{tr}(K(K + \lambda_K I)^{-1})/(nm) + n^{-1}} + J \sqrt{\lambda_K/2}$ with probability at least $1 - 2\nu$.

Theorem 2 establishes L_2 -convergence of the FGSDAR iterates. The first bound quantifies the remaining signal in A_R^* omitted from the active set after $k+1$ iterations, while the second bound controls the estimation error $\|\mathbf{C}^{k+1} - \mathbf{C}^*\|_2$, showing geometric decay at rate γ^k plus the residual term $h(J, \lambda_K)$. The final estimation error is determined by $h(J, \lambda_K)$. These expressions delineate how the sparsity level J , the sample dimensions (n, m) , and the penalty parameter λ_K jointly govern the residual approximation error.

Compared to existing function-on-scalar regression methods with high-dimensional covariates (Chen et al., 2016; Barber et al., 2017; Cai et al., 2022), which rely on predefined basis expansions and group Lasso-type penalties for variable selection, the proposed FGSDAR method adopts an L_0 penalty within the RKHS framework. Our theoretical analysis provides a general estimation error bound applicable to various RKHSs, which reduces to known results under specific conditions. For instance, if the kernel eigenvalues satisfy $\kappa_j \asymp j^{-2\alpha}$, then $\text{tr}(K(K + \lambda_K I)^{-1}) = O(\lambda_K^{-1/(2\alpha)})$. When m is small, the optimal tuning is $\lambda_K = (\log(p)/(nmJ))^{2\alpha/(2\alpha+1)}$, which yields $h(J, \lambda_K) = O\left(J(\log(p)/(nmJ))^{\alpha/(2\alpha+1)}\right)$. For large m , it simplifies to $h(J, \lambda_K) = O\left(\sqrt{J \log(p)/n}\right)$, which recovers the existing results (Barber et al., 2017; Parodi and Reimherr, 2018) if $J = J_z^*$.

Second, we provide nonasymptotic error bounds for both the scalar and functional coefficient estimates in the outcome model. These results parallel those of Li et al. (2024), which analyzed a high-dimensional, partially functional linear regression framework.

Theorem 3. *Under Assumptions 1–8, and using independent splits to fit the exposure and outcome models, let $\check{\gamma} < 1$ be defined in terms of $\theta_{J,J}$ and $c_-(J)$. Then for any $\nu \in (0, 1/5)$, with probability at least $1 - 5\nu$, the following hold:*

$$\|\beta^*|_{A^* \setminus A^{k+1}}\|_2 \leq \check{\gamma}^{k+1} \|\beta^*\|_2 + \frac{\check{\gamma}}{(1 - \check{\gamma})\theta_{J,J}} \varepsilon_1, \quad \|\beta^{k+1} - \beta^*\|_2 \leq \left(1 + \frac{\theta_{J,J}}{c_-(J)}\right) \check{\gamma}^k \|\beta^*\|_2 + b \varepsilon_1$$

for some constant $b > 0$, where $\varepsilon_1 = \sqrt{8J M_3 \log(2p/\nu)/n} + \sigma_\epsilon \sqrt{4J \log(2p/\nu)/n}$, and M_3, M_4 are defined in (??) of the supplement. Next, define $T = K^{1/2} C K^{1/2}$ and $C(s, t) = \mathbb{E}\{\tilde{\mathbf{Z}}(s)\tilde{\mathbf{Z}}(t)\}$. If $\tilde{\mathbf{Z}}^*$ is an independent copy of $\tilde{\mathbf{Z}}$ and E^* is the expectation taken over $\tilde{\mathbf{Z}}^*$, then $\mathbb{E}^* \langle \hat{\mathbf{B}} - \mathbf{B}^*, \tilde{\mathbf{Z}}^* \rangle^2 = O(\lambda + J\varepsilon_1^2 + \text{tr}(T(T + \lambda I)^{-1})/n)$. Moreover, if B^* is smoother than the RKHS \mathcal{K} , then $\|\hat{\mathbf{B}} - \mathbf{B}^*\|_{\mathcal{K}}^2 = O(\lambda + J\varepsilon_1^2 + \text{tr}(T(T + \lambda I)^{-2})/n)$.

Theorem 3 quantifies the estimation error for the outcome-model coefficients at each FGSDAR iteration. In particular, the error in estimating the scalar controls β scales as

$O(\sqrt{J \log(p)/n})$, which attains the minimax optimal rate when $J = J_y^*$ (Raskutti et al., 2011). For the functional causal effect $\mathbf{B}(t)$, we operate within a general RKHS framework and derive a prediction-error bound involving the term $\text{tr}(T(T + \lambda I)^{-1})$, often interpreted as the “effective dimension” in learning theory (Zhang, 2005). Under additional smoothness conditions on $\mathbf{B}(t)$, this prediction guarantee can be strengthened to convergence in the RKHS norm, echoing the classic result of Yuan and Cai (2010) that prediction in functional linear models is generally more tractable than full functional estimation.

Before stating the null-limit theorem for the test statistic S_n , we introduce some spectral notation. By Mercer’s Theorem, the integral operator R admits the decomposition $R(s, t) = \sum_{j=1}^{\infty} \tilde{s}_j \varphi_j(s) \varphi_j(t)$, where $\tilde{s}_1 > \tilde{s}_2 > \dots$ are its eigenvalues and $\{\varphi_j\}$ are the corresponding orthonormal eigenfunctions. With this notation in hand, we can now characterize the limiting null distribution of S_n .

Theorem 4. *Suppose Assumptions 1–8 hold. Under the null hypothesis $\mathbf{B}^*(t) \equiv 0$, the test statistic S_n converges in distribution to $\sum_{j=1}^{\infty} \tilde{s}_j x_j^2$, where $\{\tilde{s}_j\}$ are the eigenvalues of the operator R and the x_j are independent $N(0, 1)$ random variables.*

Theorem 4 shows that under H_0 , S_n converges to a weighted sum of independent χ_1^2 variables in distribution. For practical use, we approximate this null distribution by a scaled chi-square $\kappa \chi_{\zeta}^2$ via Welch–Satterthwaite moment matching: $\zeta = (\sum_j \tilde{s}_j)^2 / \sum_j \tilde{s}_j^2$ and $\kappa = \sum_j \tilde{s}_j^2 / \sum_j \tilde{s}_j$. Rather than estimating each \tilde{s}_j directly, we use the sample operator R_n to compute $\hat{\zeta} = \text{tr}(R_n)^2 / \text{tr}(R_n^2)$ and $\hat{\kappa} = \text{tr}(R_n^2) / \text{tr}(R_n)$. When there are no scalar confounders ($A^* = \emptyset$), the operator R simplifies to $R = K^{1/2} E\{\mathbf{Z}_i(s) \mathbf{Z}_i(t)\} K^{1/2}$ (Cai and Yuan, 2011; Cai et al., 2022; Li et al., 2024). In that case, our test statistic also applies directly to the standard partial functional linear model by replacing $\widehat{\mathbf{Z}}(t)$ with $\mathbf{Z}(t)$ in (8).

5 Simulation Studies

We assess the finite-sample performance of our estimator in four settings as follows.

Example 1. In the first, we consider a one-dimensional functional effect $B(t)$. We simulate each subject's data as follows. The functional covariate combines five scalar predictors and two random coefficients as $\mathbf{Z}_i(t) = \sum_{\ell=1}^5 X_{i\ell} C_\ell(t) + \tilde{\xi}_{i1} \varphi_1(t) + \tilde{\xi}_{i2} \varphi_2(t)$, where the scalar covariates \mathbf{X}_i follow a multivariate normal distribution with an AR(1) correlation $\text{corr}(X_{ij}, X_{ik}) = \rho_1^{|j-k|}$ and the coefficient functions C_1, \dots, C_5 are

$$C_1(t) = 2t^2, \quad C_2(t) = \cos(3\pi t/2 + \pi/2), \quad C_3(t) = \sqrt{2} \sin(\pi t/2) + 3\sqrt{2} \sin(3\pi t/2)$$

$$C_4(t) = 25 \exp(-t), \quad C_5(t) = 5 + 7t.$$

Moreover, the functional effect is $B(t) = \sum_{k=1}^{10} 4(-1)^{k+1} k^{-2} \varphi_k(t)$, where the orthonormal basis functions are $\varphi_{2k-1}(t) = \sqrt{2} \cos((2k-1)\pi t)$ and $\varphi_{2k}(t) = \sqrt{2} \sin((2k-1)\pi t)$ for $k = 1, \dots, 5$. We only observe $\mathbf{Z}_i(t_{ij})$ at 100 equally spaced points in $[0, 1]$. We then generate the response $Y_i = \sum_{k=1}^p X_{ik} \beta_k + \int_0^1 Z_i(t) B(t) dt + \epsilon_i$, using the true coefficient vector $\beta = (7, 0, 0, 0, 0, 5.5, 4, 3.5, 5, 4.5, \underbrace{0, \dots, 0}_{p-10})^\top$. The random components $\tilde{\xi}_{i1}$, $\tilde{\xi}_{i2}$, and ϵ_i are jointly Gaussian with variances $\text{Var}(\tilde{\xi}_{i1}) = 1$, $\text{Var}(\tilde{\xi}_{i2}) = 0.64$, and $\text{Var}(\epsilon_i) = 1$. Their covariances are $\text{Cov}(\tilde{\xi}_{i1}, \tilde{\xi}_{i2}) = 0$, $\text{Cov}(\tilde{\xi}_{i1}, \epsilon_i) = \rho_2$, and $\text{Cov}(\tilde{\xi}_{i2}, \epsilon_i) = 0.8 \rho_2$, ensuring ϵ_i is correlated with the functional covariate. Under this setup, we have $\mathcal{C} = \{1\}$, $\mathcal{P} = \{6, 7, 8, 9, 10\}$, $\mathcal{I} = \{2, 3, 4, 5\}$, and the set of irrelevant variables $\mathcal{S} = \{11, \dots, p\}$.

We conducted simulations with $n = 200$ observations under two scenarios for the scalar coefficient dimension: a low-dimensional case ($p = 20$) and a high-dimensional case ($p = 500$). In each scenario, we compared our estimator to a baseline method that ignores endogeneity—denoted “PFLR”—which directly fits the partially functional linear model.

All results are averaged over 100 Monte Carlo replicates, implemented in R 3.6.0 on

a Linux server (Intel Xeon E5-2640 v4 @ 2.40 GHz, 125 GB RAM). For each method, we evaluate $\text{MSE}_\beta = \|\hat{\beta} - \beta\|_2^2$ and $\text{MSE}_\mathbf{B} = \|\hat{\mathbf{B}} - \mathbf{B}\|_2^2$ to assess estimation accuracy of the scalar coefficients β and the functional effect \mathbf{B} . We also record variable-selection performance via FZ_Z and FZ_Y , which are the number of false zeros among scalar predictors for the functional covariate and the outcome, respectively, and FN_Z and FN_Y , which are the number of false nonzeros for those same sets. Finally, predictive accuracy is measured by the mean squared error (PMSE) on an independent test set of 200 observations.

Table 1 reports variable-selection performance and estimation accuracy for the outcome model. When endogeneity is mild (small ρ_2), our method and the naive PFLR estimator perform similarly. As ρ_2 increases, however, PFLR's errors grow substantially, whereas our method maintains low mean squared errors for both scalar and functional coefficients. In particular, our approach achieves far more reliable variable selection—fewer false nonzeros and essentially zero false exclusions of true predictors—demonstrating both higher accuracy and greater stability than PFLR.

Table 2 presents the functional exposure-model errors under varying covariate-correlation settings. Once again, our estimator consistently delivers accurate surface estimates. Results for $p = 500$ (see Section ?? of the Supplement) mirror these findings: in high-dimensional settings with endogeneity, our method substantially outperforms PFLR while still providing precise estimates for both the outcome and exposure models.

Example 2. In the second, we extend to a two-dimensional surface $\mathbf{B}(t_1, t_2)$. We generate two-dimensional $\mathbf{Z}_i(t_1, t_2)$ as $\mathbf{Z}_i(t_1, t_2) = \sum_{l=1}^5 X_{ij} C_l(t_1, t_2) + \tilde{\xi}_{i1} \varphi_1(t_1, t_2) + \tilde{\xi}_{i2} \varphi_2(t_1, t_2)$ and set $\mathbf{B}(t_1, t_2) = \exp(-(t_1 - t_2))$, where $C_1(t) = 2(t_1^2 + t_2^2)$, $C_2(t) = 3 \cos(\pi t_1/2) \cos(\pi t_2/2)$,

$$C_3(t) = \frac{\sqrt{2}}{2} \{\sin(\pi t_1/2) + 3 \sin(3\pi t_2/2)\}, C_4(t) = \exp(-(t_1 - t_2)), \quad C_5(t) = 2 + t_1 + t_2.$$

The random bases are $\varphi_1 = 1.588 \sin(\pi t_1)$ and $\varphi_2 = 2.157 \{\cos(\pi t_2) - 0.039\}$. Scalar

Table 1: Monte Carlo averages and empirical standard errors in parentheses in Example 1.

ρ_1	ρ_2		FZ_Z	FN_Z	FZ_Y	FN_Y	MSE_B	MSE_β
0.3	0	FLSEM	0.0(0.0)	0.0(0.0)	0.0(0.0)	0.393(0.486)	0.009(0.004)	0.050(0.022)
		PFLM	-	-	0.0(0.0)	2.538(1.291)	0.007(0.002)	0.077(0.028)
	0.2	FLSEM	0.0(0.0)	0.0(0.0)	0.0(0.0)	0.345(0.472)	0.008(0.003)	0.051(0.026)
		PFLM	-	-	0.0(0.0)	3.178(0.999)	0.036(0.017)	0.130(0.053)
0.5	0	FLSEM	0.0(0.0)	0.0(0.0)	0.0(0.0)	0.332(0.468)	0.008(0.003)	0.065(0.029)
		PFLM	-	-	0.0(0.0)	3.894(0.444)	0.486(0.126)	3.618(1.495)
	0.7	FLSEM	0.0(0.0)	0.0(0.0)	0.0(0.0)	0.338(0.470)	0.008(0.003)	0.073(0.031)
		PFLM	-	-	0.0(0.0)	3.961(0.396)	1.166(0.130)	9.634(1.079)
0.5	0	FLSEM	0.0(0.0)	0.198(0.397)	0.0(0.0)	0.399(0.488)	0.010(0.005)	0.060(0.027)
		PFLM	-	-	0.0(0.0)	2.339(1.266)	0.006(0.002)	0.091(0.035)
	0.2	FLSEM	0.0(0.0)	0.176(0.379)	0.0(0.0)	0.292(0.452)	0.009(0.005)	0.065(0.035)
		PFLM	-	-	0.0(0.0)	3.080(1.059)	0.035(0.015)	0.148(0.056)
0.5	0	FLSEM	0.0(0.0)	0.213(0.408)	0.0(0.0)	0.309(0.459)	0.010(0.005)	0.076(0.037)
		PFLM	-	-	0.0(0.0)	3.855(0.490)	0.474(0.132)	3.531(1.545)
	0.7	FLSEM	0.0(0.0)	0.216(0.410)	0.0(0.0)	0.281(0.446)	0.010(0.005)	0.087(0.044)
		PFLM	-	-	0.0(0.0)	3.961(0.396)	1.166(0.130)	9.622(1.075)

Table 2: Simulation results for the functional response of Monte Carlo averages and empirical standard errors in parentheses in Example 1.

ρ_1	ρ_2		MSE_{C_1}	MSE_{C_2}	MSE_{C_3}	MSE_{C_4}	MSE_{C_5}	$PMSE_Z$
0.3	0	0.005(0.004)	0.006(0.004)	0.006(0.004)	0.005(0.003)	0.005(0.004)	1.621(0.196)	
		0.005(0.004)	0.005(0.004)	0.005(0.004)	0.005(0.003)	0.005(0.003)	1.613(0.188)	
		0.005(0.004)	0.005(0.004)	0.005(0.003)	0.006(0.004)	0.005(0.004)	1.612(0.190)	
		0.005(0.003)	0.005(0.004)	0.006(0.004)	0.005(0.004)	0.005(0.004)	1.606(0.187)	
0.5	0	0.006(0.004)	0.007(0.005)	0.007(0.005)	0.009(0.007)	0.005(0.004)	1.625(0.195)	
		0.006(0.004)	0.007(0.005)	0.008(0.006)	0.008(0.006)	0.006(0.005)	1.622(0.188)	
		0.005(0.004)	0.007(0.005)	0.008(0.006)	0.009(0.006)	0.006(0.004)	1.617(0.191)	
		0.005(0.004)	0.007(0.005)	0.008(0.006)	0.008(0.005)	0.006(0.005)	1.611(0.187)	

Table 3: Simulation results of Monte Carlo averages for the outcome in Example 2.

ρ_1	ρ_2		FZ _Z	FN _Z	FZ _Y	FN _Y	MSE _B	MSE _{β}
0.3	0	FLSEM	0.0(0.0)	7.120(1.996)	0.0(0.0)	0.080(0.274)	0.049(0.014)	0.027(0.019)
		PFLM	-	-	0.0(0.0)	2.300(1.216)	0.053(0.021)	0.063(0.036)
0.2	FLSEM	0.0(0.0)	6.960(2.194)	0.0(0.0)	0.040(0.198)	0.051(0.016)	0.033(0.016)	
	PFLM	-	-	0.0(0.0)	3.380(0.830)	0.235(0.074)	0.579(0.238)	
0.5	FLSEM	0.0(0.0)	7.380(2.108)	0.0(0.0)	0.120(0.385)	0.047(0.015)	0.037(0.026)	
	PFLM	-	-	0.0(0.0)	3.960(0.198)	0.644(0.123)	3.296(0.524)	
0.7	FLSEM	0.0(0.0)	7.260(2.068)	0.0(0.0)	0.020(0.141)	0.048(0.013)	0.034(0.024)	
	PFLM	-	-	0.0(0.0)	4.000(0.0)	0.945(0.015)	7.226(0.169)	
0.5	0	FLSEM	0.0(0.0)	6.280(2.176)	0.0(0.0)	0.080(0.274)	0.046(0.012)	0.032(0.022)
		PFLM	-	-	0.0(0.0)	2.600(1.355)	0.059(0.028)	0.084(0.075)
0.2	FLSEM	0.0(0.0)	7.220(2.122)	0.0(0.0)	0.060(0.314)	0.047(0.013)	0.034(0.031)	
	PFLM	-	-	0.0(0.0)	3.560(0.733)	0.206(0.097)	0.552(0.288)	
0.5	FLSEM	0.0(0.0)	6.400(2.356)	0.0(0.0)	0.080(0.274)	0.042(0.010)	0.039(0.027)	
	PFLM	-	-	0.0(0.0)	3.960(0.198)	0.616(0.089)	3.503(0.522)	
0.7	FLSEM	0.0(0.0)	7.180(2.077)	0.0(0.0)	0.080(0.274)	0.047(0.014)	0.037(0.026)	
	PFLM	-	-	0.0(0.0)	4.000(0.0)	0.944(0.014)	7.217(0.172)	

covariates and errors are generated as in Example 1. We observe Z_i on a 100×150 grid over $[0, 1]^2$ and set $n = 400$ and $p = 20$, with true $\beta = (2, 0, 0, 0, 0, 5.5, 4, 3.5, 5, 4.5, 0, \dots, 0)^\top$. As before, we have $\mathcal{C} = \{1\}$, $\mathcal{P} = \{6, 7, 8, 9, 10\}$, $\mathcal{I} = \{2, 3, 4, 5\}$, and $\mathcal{S} = \{11, \dots, p\}$.

Table 3 summarizes selection accuracy, estimation, and prediction errors for these simulations. Similar to Example 1, our method outperforms PFLR across all settings. Table 4 reports functional-model errors under various correlation structures, confirming that FGS-DAR yields accurate surface estimates in high-dimensional imaging scenarios.

Example 3. In the third, we evaluate the proposed divide-and-conquer procedures under the two-dimensional design of Example 2. As shown in Figure ??, the divide-and-conquer estimator closely matches the accuracy and predictive performance of the full-sample fit. Due to page limits, detailed descriptions are deferred to Section ?? of the supplement.

Example 4. In our fourth example, we evaluate the finite-sample performance of the

Table 4: Estimation results for the two dimensional functional response in Example 2.

ρ_1	ρ_2	MSE_{C_1}	MSE_{C_2}	MSE_{C_3}	MSE_{C_4}	MSE_{C_5}	$PMSE_Z$
0.3	0	0.138(0.023)	0.139(0.024)	0.333(0.033)	0.068(0.028)	0.058(0.024)	3.381(0.159)
	0.2	0.132(0.021)	0.138(0.025)	0.334(0.041)	0.073(0.028)	0.070(0.044)	3.394(0.167)
	0.5	0.138(0.021)	0.140(0.028)	0.338(0.046)	0.068(0.018)	0.068(0.038)	3.389(0.159)
	0.7	0.137(0.025)	0.138(0.020)	0.336(0.039)	0.069(0.024)	0.063(0.029)	3.399(0.157)
0.5	0	0.139(0.030)	0.136(0.025)	0.336(0.035)	0.067(0.023)	0.068(0.039)	3.410(0.175)
	0.2	0.135(0.023)	0.136(0.020)	0.332(0.029)	0.066(0.023)	0.070(0.041)	3.392(0.150)
	0.5	0.138(0.027)	0.141(0.018)	0.330(0.032)	0.074(0.027)	0.069(0.038)	3.393(0.129)
	0.7	0.136(0.026)	0.143(0.023)	0.329(0.031)	0.074(0.028)	0.070(0.048)	3.377(0.150)

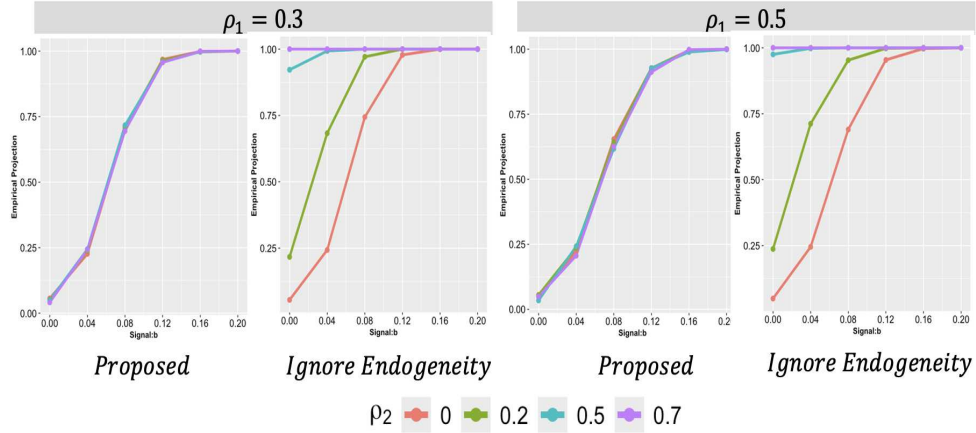


Figure 2: Empirical rejection of proposed testing method, “Ignore endogeneity” indicates using the observed functional data for testing.

proposed hypothesis test. We retain the design of Example 1 but scale the true functional effect to $B(t) = b \sum_{k=1}^5 (-1)^{k+1} k^{-2} \varphi_k(t)$ with $b \in \{0, 0.04, 0.08, 0.12, 0.16, 0.20\}$.

Figure 2 reports empirical rejection rates at the 5% significance level for our method and for a naive test that treats the functional covariate as observed without correcting for endogeneity, based on 1,000 simulations. When endogeneity is absent ($\rho_2 = 0$), the naive test correctly controls size. As ρ_2 increases, however, its Type I error inflates substantially, making its results unreliable. In contrast, our test maintains size near 5% across all ρ_2 levels, and its power approaches 100% as the signal strength b grows.

6 Real Data Analysis of UK Biobank

The UK Biobank is a large-scale, prospective cohort study that recruited over 500,000 participants aged 40–69 from across the United Kingdom between 2006 and 2010 (Sudlow et al., 2015). One of its primary objectives is to collect comprehensive health and biological data prior to disease onset (Elliott et al., 2018), thereby enabling the investigation of early predictors of complex traits and diseases.

Among the rich set of variables available, fluid intelligence scores are derived from participants' performance on 13 problem-solving questions, representing a core component of cognitive function. Meanwhile, brain function is typically assessed through task-based fMRI, which captures dynamic patterns of neural activation. Prior research has highlighted associations between structural and functional brain imaging and intelligence (Cheng et al., 2020), with findings suggesting that individuals with larger brain volumes tend to perform better on intelligence tests (McDaniel, 2005; Rushton and Ankney, 2009).

The central goal of our data analysis is to investigate how genetic variations and brain functional networks jointly influence individual differences in fluid intelligence. By integrating single-nucleotide polymorphism (SNP) data with fMRI measurements, we aim to (i) identify neural activation patterns and brain regions correlated with fluid intelligence, (ii) uncover genetic variants associated with these traits, and (iii) determine shared SNPs that may serve as confounders or mediators. This integrative approach offers critical insights into the neurobiological and genetic underpinnings of human intelligence. Ultimately, such findings could inform the design of targeted educational interventions, improve strategies for supporting cognitive development, and enhance early detection of cognitive impairments.

After rigorous quality control of both imaging and phenotypic data, we constructed an analytical dataset of $n=11,400$ participants. This dataset includes a comprehensive

set of covariates: demographic factors (age, sex, education level, body mass index, social deprivation index), lifestyle variables (smoking, physical activity, healthy diet, moderate alcohol consumption), medical history (hypertension, diabetes), imaging-related technical variables (site, volumetric scaling, head position, brain position), and interaction terms (age·sex, age^2 , sex· age^2). To correct for population stratification, we additionally include the top 40 principal components from genome-wide SNP data (Price et al., 2006). Resting-state functional connectivity fMRI serves as the imaging data that measures brain activity, summarized by 78 grid points. Each grid point represents the functional connectivity between a pair of brain networks or regions. These regions are grouped into 12 canonical resting-state networks, with detailed labels shown in Figure 3(b).

Given the ultrahigh dimensionality of the SNP data—over 96 million variants—we apply a two-step sure independence screening (SIS) procedure (Fan and Lv, 2008), separately tailored for both the outcome (fluid intelligence) and imaging (fMRI) models. Specifically, we control for covariates and rank SNPs based on their marginal absolute correlations with the fluid intelligence score, retaining the top 2,000. For the imaging model, we conduct marginal screening across all fMRI voxels and rank SNPs by the aggregated absolute correlation across pixels, again retaining the top 2,000 SNPs. All SNPs and continuous variables are standardized for comparability.

This screening strategy aligns with practices from genome-wide association studies (GWAS), which aim to detect associations between genetic variants and phenotypes at scale. Table ?? in the supplement presents the SNPs commonly selected in both the fluid intelligence and fMRI screening processes. Notably, these SNPs cluster within the same linkage disequilibrium (LD) block on chromosome 15 (Berisa and Pickrell, 2016), suggesting a shared genetic influence on both brain function and cognition.

Figure 3(a) provides a genomic ideogram of SNPs selected by our proposed FLSEM and PFLM. FLSEM selects 158 SNPs, PFLM selects 163, with 126 SNPs overlapping. Most of the shared SNPs are located on chromosomes 2, 6, and 14, highlighting potential key genomic regions that contribute to individual differences in cognitive ability through both direct and indirect pathways.

Building on the leading SNPs identified through the sure independence screening, our analysis proceeds in three main steps. First, we fit an imaging-on-scalar model to estimate the imaging variables as a function of the selected genetic variants. This step captures the component of brain activation explained by the SNPs. Second, using the fitted imaging values as covariates, we apply a variable selection model to the fluid intelligence scores to identify SNPs that directly influence cognition after accounting for imaging-based effects. Finally, we estimate the direct effect of the imaging variables on fluid intelligence, adjusting for demographic, clinical, and genetic confounders, and the selected precision variables.

Figure 3(b) illustrates the estimated effects of fMRI-based brain connectivity on fluid intelligence derived from both the proposed FLSEM and the PFLM. The results reveal distinct patterns across methods. Notably, both models identify positive associations between connectivity in the language and ventral multimodal networks and higher fluid intelligence scores. However, connectivity involving the visual network displays divergent effects between the two models, suggesting method-dependent sensitivity to specific brain regions.

To formally evaluate the role of brain function in cognitive performance, we test the association between fMRI-derived imaging exposures and fluid intelligence scores. The proposed testing procedure yields a p -value of 0.08, indicating marginal significance at the 10% level. To further probe the generalizability of these associations, we extend our analysis to other cognitive phenotypes available in the UK Biobank, including: Reaction Time (assess-

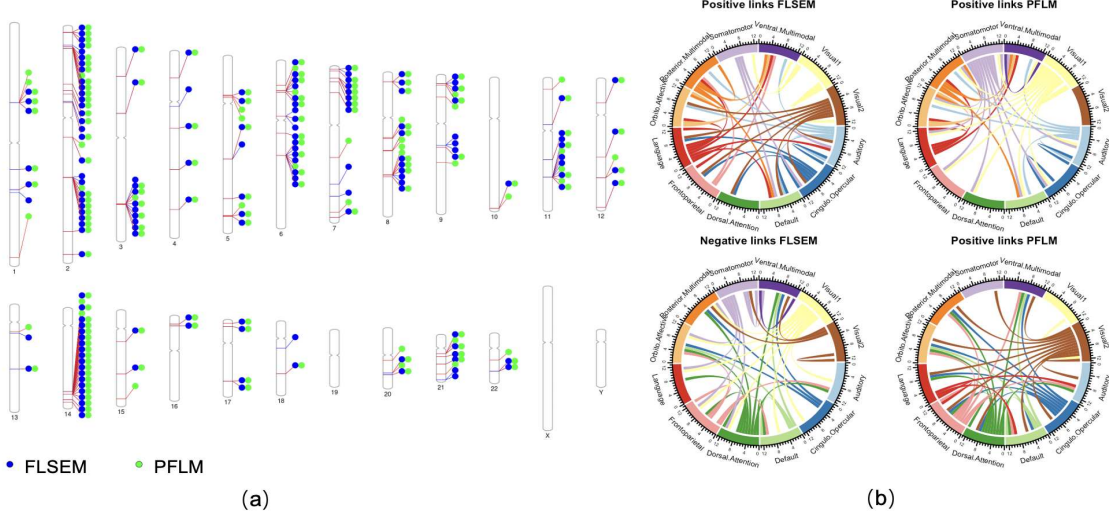


Figure 3: Panel (a) shows the positions of SNPs selected by FLSEM and PFLM; Panel (b) displays the positive and negative fMRI effect estimates on fluid intelligence from both methods.

ing processing speed), Trail Making (executive function and cognitive flexibility), Numeric Memory (working memory), Matrix Completion (reasoning and pattern recognition), and Tower Rearranging (planning and problem-solving). Significant associations are found for Reaction Time ($p = 0.003$), Trail Making ($p = 0.001$), and Tower Rearranging ($p = 0.009$), while Matrix Completion is marginally significant ($p = 0.087$). In contrast, Numeric Memory ($p = 0.268$) shows no significant relationship with the imaging data. These findings underscore the heterogeneous influence of brain function on different aspects of cognition and emphasize the need for targeted, phenotype-specific modeling.

7 Discussion

We introduced the FLSEM framework to uncover causal links among genetic, imaging, and clinical data under unobserved confounding. Our L_0 -penalized, three-step estimator—bolstered by the FGSDAR algorithm—simultaneously handles endogeneity, high-dimensional scalars, and infinite-dimensional functions. We proved identification for mixed scalar–functional

instruments, derived nonasymptotic error and testing guarantees, and demonstrated via simulations that our approach outperforms naive methods, especially under strong endogeneity. An application to the UK Biobank confirms its practical value in large-scale multimodal studies. The current framework can be extended to incorporate GWAS summary data for causal factor identification (Fang et al., 2025), and to enable causal mediation analysis by modeling both direct and mediated treatment effects (Yang et al., 2024).

8 Acknowledgment

This research has been conducted using the UK Biobank Resource under Application Number 22783, subject to a data transfer agreement. We thank the participants in the UKB study for their contribution and the research teams for the work in collecting, processing, and disseminating these datasets for analysis. We thank the University of North Carolina at Chapel Hill and the Research computing groups for providing computational resources and support that have contributed to the research results. This paper was primarily completed during Dr. Ting Li’s visit to UNC Chapel Hill. Dr. Fan’s work was partially supported by the National Science Foundation (NSF) grants DMS-2230795 and DMS-2230797. Dr. Zhu’s work was partially supported by the Gillings Innovation Laboratory on generative AI and by grants from the National Institute on Aging (NIA) of the National Institutes of Health (NIH), including 1R01AG085581, and RF1AG082938, the National Institute of Mental Health (NIMH) grant 1R01MH136055, and the NIH grants R01AR082684, and 1OT2OD038045-01. The content of this paper is solely the responsibility of the authors and does not necessarily represent the official views of these institutions.

9 Author Contributions

Ting Li proposed the statistical method, conducted the theoretical analysis and simulation studies, and drafted the manuscript. Ethan Fang assisted with the theoretical analysis and contributed to revising and editing the manuscript. Tengfei Li performed the real data analysis and contributed to the interpretation of empirical results. Hongtu Zhu, supervised the project, provided critical guidance throughout the research process, and revised the manuscript. All authors read and approved the final version of the manuscript.

References

Babii, A. (2022). High-dimensional mixed-frequency iv regression. *Journal of Business & Economic Statistics* 40(4), 1470–1483.

Barber, R. F., M. Reimherr, and T. Schill (2017). The function-on-scalar lasso with applications to longitudinal gwas. *Electronic Journal of Statistics* 11(1), 1351–1389.

Berisa, T. and J. K. Pickrell (2016). Approximately independent linkage disequilibrium blocks in human populations. *Bioinformatics* 32(2), 283.

Burgess, S., D. S. Small, and S. G. Thompson (2017). A review of instrumental variable estimators for mendelian randomization. *Statistical Methods in Medical Research* 26(5), 2333–2355.

Cai, T. T. and M. Yuan (2011). Optimal estimation of the mean function based on discretely sampled functional data: Phase transition. *The Annals of Statistics* 39(5), 2330–2355.

Cai, T. T. and M. Yuan (2012). Minimax and adaptive prediction for functional linear regression. *Journal of the American Statistical Association* 107(499), 1201–1216.

Cai, X., L. Xue, J. Cao, and A. D. N. Initiative (2022). Robust estimation and variable selection for function-on-scalar regression. *Canadian Journal of Statistics* 50(1), 162–179.

Cardot, H., F. Ferraty, and P. Sarda (2003). Spline estimators for the functional linear model. *Statistica Sinica*, 571–591.

Chen, C., S. Guo, and X. Qiao (2022). Functional linear regression: dependence and error contamination. *Journal of Business & Economic Statistics* 40(1), 444–457.

Chen, Y., J. Goldsmith, and R. T. Ogden (2016). Variable selection in function-on-scalar regression. *Stat* 5(1), 88–101.

Cheng, S., C. Wu, X. Qi, L. Liu, M. Ma, L. Zhang, B. Cheng, C. Liang, P. Li, O. P. Kafle, et al. (2020). A large-scale genetic correlation scan between intelligence and brain imaging phenotypes. *Cerebral Cortex* 30(7), 4197–4203.

Dorn, M., M. Birke, and C. Jentsch (2022). Testing exogeneity in the functional linear regression model. *arXiv preprint arXiv:2208.06842*.

Elliott, L. T., K. Sharp, F. Alfaro-Almagro, S. Shi, K. L. Miller, G. Douaud, J. Marchini, and S. M. Smith (2018). Genome-wide association studies of brain imaging phenotypes in UK Biobank. *Nature* 562(7726), 210–216.

Engl, H. W., M. Hanke, and A. Neubauer (1996). *Regularization of inverse problems*. Springer Science & Business Media.

Fan, J. and J. Lv (2008). Sure independence screening for ultra-high dimensional feature space. *Journal of the Royal Statistical Society: Series B (Statistical Methodology)* 70(5), 849–911.

Fan, Z. and M. Reimherr (2017). High-dimensional adaptive function-on-scalar regression. *Econometrics and statistics* 1, 167–183.

Fang, L., H. Xue, Z. Lin, and W. Pan (2025). Multivariate proteome-wide association study to identify causal proteins for alzheimer disease. *The American Journal of Human Genetics* 112(2), 291–300.

Florens, J.-P. and S. Van Bellegem (2015). Instrumental variable estimation in functional linear models. *Journal of Econometrics* 186(2), 465–476.

Guo, Z., H. Kang, T. Tony Cai, and D. S. Small (2018). Confidence intervals for causal effects with invalid instruments by using two-stage hard thresholding with voting. *Journal of the Royal Statistical Society Series B: Statistical Methodology* 80(4), 793–815.

He, G., H. Müller, and J. Wang (2000). Extending correlation and regression from multivariate to functional data. *Asymptotics in statistics and probability: papers in honor of George Gregory Roussas*, 197.

Hong, C., Y. Wang, and T. Cai (2022). A divide-and-conquer method for sparse risk prediction and evaluation. *Biostatistics* 23(2), 397–411.

Hsing, T. and R. Eubank (2015). *Theoretical foundations of functional data analysis, with an introduction to linear operators*, Volume 997. John Wiley & Sons.

Huang, J., Y. Jiao, Y. Liu, and X. Lu (2018). A constructive approach to l0 penalized regression. *The Journal of Machine Learning Research* 19(1), 403–439.

Hudson, R. R. and N. L. Kaplan (1988). The coalescent process in models with selection and recombination. *Genetics* 120(3), 831–840.

Jack Jr, C. R., D. S. Knopman, W. J. Jagust, R. C. Petersen, M. W. Weiner, P. S. Aisen, L. M. Shaw, P. Vemuri, H. J. Wiste, S. D. Weigand, et al. (2013). Tracking pathophysiological processes in alzheimer’s disease: an updated hypothetical model of dynamic biomarkers. *The Lancet Neurology* 12(2), 207–216.

Jack Jr, C. R., D. S. Knopman, W. J. Jagust, L. M. Shaw, P. S. Aisen, M. W. Weiner, R. C. Petersen, and J. Q. Trojanowski (2010). Hypothetical model of dynamic biomarkers of the Alzheimer’s pathological cascade. *The Lancet Neurology* 9(1), 119–128.

Jadhav, S., C. D. Tekwe, and Y. Luan (2022). A function-based approach to model the measurement error in wearable devices. *Statistics in Medicine* 41(24), 4886–4902.

Kang, H., A. Zhang, T. T. Cai, and D. S. Small (2016). Instrumental variables estimation with some invalid instruments and its application to mendelian randomization. *Journal of the American statistical Association* 111(513), 132–144.

Kong, D., B. An, J. Zhang, and H. Zhu (2019). L2rm: Low-rank linear regression models for high-dimensional matrix responses. *Journal of the American Statistical Association*.

Kong, D., K. Xue, F. Yao, and H. H. Zhang (2016). Partially functional linear regression in high dimensions. *Biometrika* 103(1), 147–159.

Lawlor, D. A., R. M. Harbord, J. A. Sterne, N. Timpson, and G. Davey Smith (2008). Mendelian randomization: using genes as instruments for making causal inferences in epidemiology. *Statistics in medicine* 27(8), 1133–1163.

Le, B. D. and J. L. Stein (2019). Mapping causal pathways from genetics to neuropsychiatric disorders using genome-wide imaging genetics: Current status and future directions. *Psychiatry and clinical neurosciences* 73(7), 357–369.

Li, T., Y. Yu, J. Marron, and H. Zhu (2024). A partially functional linear regression framework for integrating genetic, imaging, and clinical data. *The Annals of Applied Statistics* 18(1), 704–728.

Li, T. and Z. Zhu (2020). Inference for generalized partial functional linear regression. *Statistica Sinica* 30, 1379–1397.

Lian, H. and Z. Fan (2018). Divide-and-conquer for debiased l1-norm support vector machine in ultra-high dimensions. *Journal of Machine Learning Research* 18(182), 1–26.

Liang, X., E. Sanderson, and F. Windmeijer (2022). Selecting valid instrumental variables in linear models with multiple exposure variables: adaptive lasso and the median-of-medians estimator. *arXiv preprint arXiv:2208.05278*.

McDaniel, M. A. (2005). Big-brained people are smarter: A meta-analysis of the relationship between in vivo brain volume and intelligence. *Intelligence* 33(4), 337–346.

Mirshani, A. and M. Reimherr (2021). Adaptive function-on-scalar regression with a smoothing elastic net. *Journal of Multivariate Analysis* 185, 104765.

Parodi, A. and M. Reimherr (2018). Simultaneous variable selection and smoothing for high-dimensional function-on-scalar regression. *Electronic Journal of Statistics* 12(2), 4602–4639.

Price, A. L., N. J. Patterson, R. M. Plenge, M. E. Weinblatt, N. A. Shadick, and D. Reich (2006). Principal components analysis corrects for stratification in genome-wide association studies. *Nature genetics* 38(8), 904–909.

Raskutti, G., M. J. Wainwright, and B. Yu (2011). Minimax rates of estimation for high-dimensional linear regression over ℓ_q -balls. *IEEE transactions on information theory* 57(10), 6976–6994.

Rushton, J. P. and C. D. Ankney (2009). Whole brain size and general mental ability: a review. *International Journal of Neuroscience* 119(5), 692–732.

Sanderson, E., M. M. Glymour, M. V. Holmes, H. Kang, J. Morrison, M. R. Munafò, T. Palmer, C. M. Schooling, C. Wallace, Q. Zhao, et al. (2022). Mendelian randomization. *Nature Reviews Methods Primers* 2(1), 6.

Seong, D. and W.-K. Seo (2022). Functional instrumental variable regression with an application to estimating the impact of immigration on native wages. *arXiv preprint arXiv:2110.12722*.

Shin, H. (2009). Partial functional linear regression. *Journal of Statistical Planning and Inference* 139(10), 3405–3418.

Sudlow, C., J. Gallacher, N. Allen, V. Beral, P. Burton, J. Danesh, P. Downey, P. Elliott, J. Green, M. Landray, et al. (2015). Uk biobank: an open access resource for identifying the causes of a wide range of complex diseases of middle and old age. *PLoS medicine* 12(3), e1001779.

Taschler, B., S. M. Smith, and T. E. Nichols (2022). Causal inference on neuroimaging data with mendelian randomisation. *NeuroImage* 258, 119385.

Tekwe, C. D., R. S. Zoh, M. Yang, R. J. Carroll, G. Honvoh, D. B. Allison, M. Benden, and L. Xue (2019). Instrumental variable approach to estimating the scalar-on-function regression model with measurement error with application to energy expenditure assessment in childhood obesity. *Statistics in medicine* 38(20), 3764–3781.

Vandenbroucke, J. P. (2004). When are observational studies as credible as randomised trials? *The Lancet* 363(9422), 1728–1731.

Wahba, G. (1990). *Spline models for observational data*, Volume 59 of *CBMS-NSF Regional Conference Series in Applied Mathematics*. Society for Industrial and Applied Mathematics (SIAM), Philadelphia, PA.

Wang, Y. (2011). *Smoothing splines: methods and applications*. CRC press.

Xu, Y. and J. Kang (2023). Bayesian image mediation analysis. *arXiv preprint arXiv:2310.16284*.

Xu, Y., S. Yang, and J. Kang (2024). Bayesian structured mediation analysis with unobserved confounders. *arXiv preprint arXiv:2407.04142*.

Yang, H., Z. Liu, R. Wang, E.-Y. Lai, J. Schwartz, A. A. Baccarelli, Y.-T. Huang, and X. Lin (2024). Causal mediation analysis for integrating exposure, genomic, and phenotype data. *Annual Review of Statistics and Its Application* 12.

Yu, D., L. Wang, D. Kong, and H. Zhu (2022). Mapping the genetic-imaging-clinical pathway with applications to alzheimer’s disease. *Journal of the American Statistical Association* 117(540), 1656–1668.

Yuan, M. and T. T. Cai (2010). A reproducing kernel Hilbert space approach to functional linear regression. *The Annals of Statistics* 38(6), 3412–3444.

Zhang, T. (2005). Learning bounds for kernel regression using effective data dimensionality. *Neural computation* 17(9), 2077–2098.

Zhang, Y., J. Duchi, and M. Wainwright (2015). Divide and conquer kernel ridge regression: A distributed algorithm with minimax optimal rates. *The Journal of Machine Learning Research* 16(1), 3299–3340.

Zhang, Z., X. Wang, L. Kong, and H. Zhu (2022). High-dimensional spatial quantile function-on-scalar regression. *Journal of the American Statistical Association* 117(539), 1563–1578.

Zhou, S. K., H. Greenspan, C. Davatzikos, J. S. Duncan, B. Van Ginneken, A. Madabhushi, J. L. Prince, D. Rueckert, and R. M. Summers (2021). A review of deep learning in medical imaging: imaging traits, technology trends, case studies with progress highlights, and future promises. *Proceedings of the IEEE*.

Zhu, H., T. Li, and B. Zhao (2023). Statistical learning methods for neuroimaging data analysis with applications. *Annual Review of Biomedical Data Science* 6, 73–104.

Zoh, R. S., Y. Luan, and C. Tekwe (2022). A fully bayesian semi-parametric scalar-on-function regression (sofr) with measurement error using instrumental variables. *arXiv preprint arXiv:2202.00711*.

Causal Inference in Biomedical Imaging with Functional Linear Structural Equation Models

This supplementary material contains additional simulation results, additional real data analysis, auxiliary lemmas and proofs of the theorems in the main text.

S1 Additional Simulation Studies

In this section, we present additional simulation results to examine the finite sample performance of the proposed method in scenarios where the dimension of scalar covariates exceeds the sample size, and the proposed divide-and-conquer procedures.

Example 1 (Continued). The data settings are similar to those in Example 1 in the main text, with the exception that the dimension p is set to 500.

Tables S1 and S2 summarize the results, including variable selection accuracy, estimation accuracy for the outcome model, and the functional model. The findings are consistent with those observed under $p = 20$: the proposed method outperforms the PFLR method in the presence of endogeneity, while providing accurate estimates for both the outcome and exposure models.

Example 3 (Continued). In this example, we evaluate the proposed divide-and-conquer procedures under the two-dimensional design of Example 2, with $\rho_1 = 0.2$ and $\rho_2 = 0.3$.

First, we split the n observations into two equal subsamples to estimate the outcome model. Figure S1 (top row) displays boxplots of the outcome-prediction error and the MSEs for $\mathbf{B}(t_1, t_2)$ and β . Even with half the data, the divide-and-conquer estimator matches the accuracy and predictive performance of the full-sample fit.

Next, we apply the region-based divide-and-conquer scheme to estimate the functional coefficients C_1, \dots, C_5 . We tile the imaging domain into 10×10 subregions and again split the sample into two subsets. Figure S1 (bottom row) shows boxplots of the MSE for each $C_\ell(t_1, t_2)$. The subregion-based estimates incur negligible efficiency loss compared to the full data, demonstrating that both divide-and-conquer strategies scale effectively without sacrificing accuracy.

Table S1: Simulation results of Monte Carlo averages and empirical standard errors in parentheses in Example 1 for $p = 500$.

ρ_1	ρ_2		FZ_Z	FN_Z	FZ_Y	FN_Y	MSE_B	MSE_β
0.3	0	FLSEM	0.000(0.000)	1.193(0.686)	0.000(0.000)	1.875(0.896)	0.008(0.002)	0.158(0.065)
		PFLM	-	-	0.000(0.000)	3.913(0.428)	0.006(0.003)	0.194(0.036)
	0.2	FLSEM	0.000(0.000)	1.250(0.702)	0.000(0.000)	1.866(0.904)	0.010(0.004)	0.184(0.076)
		PFLM	-	-	0.000(0.000)	3.894(0.444)	0.016(0.005)	0.189(0.039)
0.5	0	FLSEM	0.000(0.000)	1.257(0.677)	0.000(0.000)	2.041(0.905)	0.009(0.003)	0.248(0.094)
		PFLM	-	-	0.000(0.000)	3.942(0.405)	0.207(0.050)	0.470(0.111)
	0.2	FLSEM	0.000(0.000)	1.243(0.686)	0.000(0.000)	2.094(0.966)	0.009(0.003)	0.275(0.107)
		PFLM	-	-	0.000(0.000)	3.923(0.421)	1.108(0.278)	8.955(3.187)
0.5	0	FLSEM	0.000(0.000)	0.476(0.497)	0.000(0.000)	1.777(1.130)	0.009(0.004)	0.153(0.079)
		PFLM	-	-	0.000(0.000)	3.856(0.508)	0.007(0.003)	0.202(0.039)
	0.2	FLSEM	0.000(0.000)	0.449(0.495)	0.000(0.000)	1.790(1.037)	0.011(0.006)	0.192(0.091)
		PFLM	-	-	0.000(0.000)	3.836(0.537)	0.019(0.008)	0.201(0.040)
0.5	0	FLSEM	0.000(0.000)	0.471(0.497)	0.000(0.000)	1.909(0.918)	0.011(0.006)	0.249(0.101)
		PFLM	-	-	0.000(0.000)	3.875(0.477)	0.197(0.067)	0.493(0.194)
	0.2	FLSEM	0.000(0.000)	0.439(0.494)	0.000(0.000)	1.925(0.943)	0.011(0.006)	0.281(0.112)
		PFLM	-	-	0.000(0.000)	3.913(0.428)	1.080(0.293)	8.595(3.449)

Table S2: Simulation results for the functional response of Monte Carlo averages and empirical standard errors in parentheses in Example 1 for $p = 500$.

ρ_1	ρ_2	MSE_{C_1}	MSE_{C_2}	MSE_{C_3}	MSE_{C_4}	MSE_{C_5}	$PMSE_Z$
0.3	0	0.004(0.003)	0.005(0.004)	0.006(0.004)	0.006(0.005)	0.006(0.005)	1.643(0.195)
	0.2	0.005(0.003)	0.006(0.004)	0.005(0.004)	0.006(0.004)	0.005(0.004)	1.634(0.191)
	0.5	0.006(0.004)	0.007(0.005)	0.006(0.004)	0.006(0.005)	0.006(0.005)	1.635(0.192)
	0.7	0.005(0.003)	0.006(0.005)	0.006(0.004)	0.005(0.004)	0.006(0.004)	1.638(0.192)
0.5	0	0.007(0.004)	0.008(0.006)	0.007(0.006)	0.007(0.005)	0.007(0.005)	1.633(0.192)
	0.2	0.006(0.004)	0.008(0.005)	0.007(0.006)	0.007(0.005)	0.007(0.005)	1.628(0.190)
	0.5	0.005(0.003)	0.008(0.006)	0.009(0.006)	0.007(0.005)	0.007(0.006)	1.627(0.189)
	0.7	0.006(0.004)	0.008(0.005)	0.008(0.006)	0.008(0.006)	0.007(0.005)	1.630(0.189)

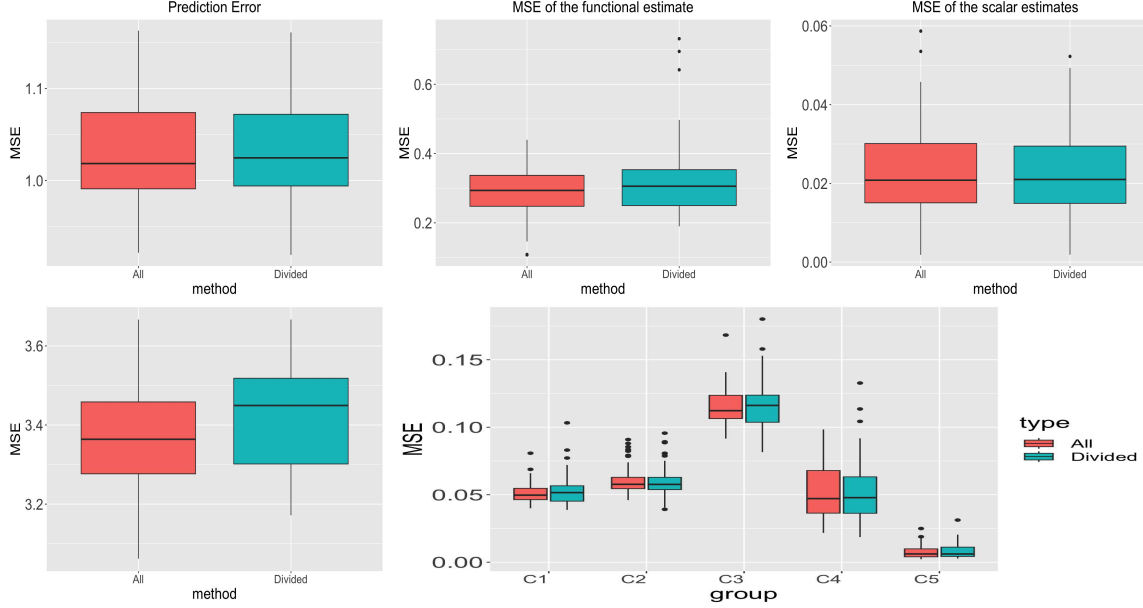


Figure S1: Boxplots of prediction errors and MSEs of Estimates for parameters in the outcome model (the first row), and for the functional model (the second row).

S2 Additional Real Data Analysis

Table S3 presents the SNPs commonly selected in both the fluid intelligence and fMRI screening processes.

Table S3: Detailed information of the common SNPs for fluid intelligence score and fMRI.

SNP	Chr	Base Pair	Allele 1	Allele 2
rs76443071	15	32943439	T	C
rs118151036	15	329454622	C	A
rs143826519	15	32947334	T	C

S3 Proofs of the main theorems

Proof of Theorem 1. Under the condition

$$\int_{\mathcal{T}} C(t) \mathbf{B}(t) dt = \sum_{k=1}^R b_k \mathbf{c}_k + O(R^{-2r})$$

for some $r > 0$, the identification of the functional parameter $\mathbf{B}(t)$ can be reduced to identifying the finite-dimensional coefficient vector $\{b_k\}_{k=1}^R$, by noting that $\mathbf{B}(t) \approx \sum_{k=1}^R b_k \varphi_k(t)$, where $\{\varphi_k(t)\}$ denotes an orthogonal basis.

We establish that β is uniquely identified if and only if $\{b_k\}_{k=1}^R$ is uniquely determined by the moment conditions in equation (4). Suppose $\{b_k\}_{k=1}^R$ is uniquely identified. Then, for any two solutions $\beta^{(1)}$ and $\beta^{(2)}$, we have:

$$\Gamma^* = \beta^{(1)} + \sum_{k=1}^R b_k \mathbf{c}_k \quad \text{and} \quad \Gamma^* = \beta^{(2)} + \sum_{k=1}^R b_k \mathbf{c}_k.$$

Subtracting the two equations yields $\beta^{(1)} = \beta^{(2)} = \Gamma^* - \sum_{k=1}^R b_k \mathbf{c}_k$, confirming the uniqueness of β . Therefore, it suffices to show that $\{b_k\}_{k=1}^R$ is uniquely identifiable.

First, we prove sufficiency. Assume there exist two solutions $(\beta^{(1)}, \{b_k^{(1)}\})$ and $(\beta^{(2)}, \{b_k^{(2)}\})$ to (4) such that

$$\Gamma^* = \beta^{(1)} + \sum_{k=1}^R b_k^{(1)} \mathbf{c}_k \quad \text{and} \quad \Gamma^* = \beta^{(2)} + \sum_{k=1}^R b_k^{(2)} \mathbf{c}_k.$$

Let $\mathcal{C}^{(d)} = \{j : \beta_j^{(d)} \neq 0\}$ denote the set of invalid instruments under $\beta^{(d)}$ for $d = 1$ and 2. Since $|\mathcal{C}^{(d)}| < U$, its complement satisfies

$$|(\mathcal{C}^{(d)})^C| = L - |\mathcal{C}^{(d)}| > L - U.$$

Choose subsets $S_1 \subset (\mathcal{C}^{(1)})^C$ and $S_2 \subset (\mathcal{C}^{(2)})^C$ of size $|S_1| = |S_2| = L - U + 1 > K$. For each $j \in S_1$ and $\nu \in S_2$, the moment equations reduce to

$$\Gamma_j^* = \sum_{k=1}^R b_k^{(1)} c_{jk} \quad \text{and} \quad \Gamma_\nu^* = \sum_{k=1}^R b_k^{(2)} c_{\nu k}.$$

By the subspace-restriction condition, it follows that $b_k^{(1)} = b_k^{(2)}$ for all k . Consequently,

$$\beta^{(1)} = \Gamma^* - \sum_{k=1}^R b_k^{(1)} \mathbf{c}_k = \Gamma^* - \sum_{k=1}^R b_k^{(2)} \mathbf{c}_k = \beta^{(2)},$$

contradicting the assumption of distinct solutions. Hence, the solution is unique.

Second, we prove necessity by showing that the subspace-restriction condition on Γ^* and $\{\mathbf{c}_k\}$ must hold if the solution is unique. Such a set always exists by taking a subset of the true valid instruments. Specifically, let \mathcal{C}^* denote the true set of invalid instruments. Since

$|(\mathcal{C}^*)^C| > L - U$, we can select a subset $(\mathcal{C}'')^C \subseteq (\mathcal{C}^*)^C$ of size $L - U + 1$ such that for each $j \in (\mathcal{C}'')^C$,

$$\Gamma_j^* = \sum_{k=1}^R b_k^{(**)'} c_{jk}.$$

If this subset $(\mathcal{C}'')^C$ is unique, the subspace-restriction condition holds trivially since $\{b_k^{(**)'}\}$ must match the true coefficients $\{b_k\}$.

Now assume there are two or more subsets. Let $\mathcal{C}^{(1)}$ and $\mathcal{C}^{(2)}$ be any two subsets of $\{1, \dots, L\}$ whose complements each have size $|(\mathcal{C}^{(d)})^C| = L - U + 1 > R$ for $d = 1, 2$. Denote by $\{b_k^{(d)}\}$ the coefficients inferred from $(\mathcal{C}^{(d)})^C$ for $d = 1, 2$ satisfying $\Gamma_j^* = \sum_{k=1}^R b_k^{(d)} c_{jk}$ for $j \in (\mathcal{C}^{(d)})^C$. We aim to show that $b_k^{(1)} = b_k^{(2)}$.

For each $d = 1, 2$, we construct two solution sets $(\beta^{(d)}, \{b_k^{(d)}\})$ to (4) for $d = 1, 2$ by taking $\beta_j^{(d)} = 0$ for $j \in (\mathcal{C}^{(d)})^C$ and $\beta_j^{(d)} = \Gamma_j^* - \sum_{k=1}^R b_k^{(d)} c_{jk}$ for $j \in \mathcal{C}^{(d)}$. It is obvious that the two solution sets satisfy

$$\begin{cases} \Gamma_j^* = \sum_{k=1}^R b_k^{(d)} c_{jk}, & j \in (\mathcal{C}^{(d)})^C, \\ \Gamma_j^* = \beta_j^{(d)} + \sum_{k=1}^R b_k^{(d)} c_{jk}, & j \in \mathcal{C}^{(d)}, \end{cases}$$

where $\beta^{(d)}$ has fewer than U nonzero entries. Uniqueness of the overall solution implies $b_k^{(1)} = b_k^{(2)}$. Since the choice of $\mathcal{C}^{(1)}$ and $\mathcal{C}^{(2)}$ was arbitrary, we conclude that $b_k^{(m)} = b_k^{(m')}$ for all m, m' , establishing necessity.

□

Proof of Corollary 1. Consider any two sets S_m and $S_{m'}$ with corresponding coefficients $\{b_k^{(m)}\}$ and $\{b_k^{(m')}\}$ satisfying

$$\sum_{k=1}^R b_k^{(m)} \mathbf{c}_{\ell k} = \Gamma_\ell^*, \quad \ell \in S_m, \quad \text{and} \quad \sum_{k=1}^R b_k^{(m')} \mathbf{c}_{\ell k} = \Gamma_\ell^*, \quad \ell \in S_{m'}.$$

We now show that $S_m \cap S_{m'}$ contains at least R elements. Since $|S_m| = |S_{m'}| = L - U + 1 \geq (L + R - 1)/2 + 1$, we have

$$|S_m| + |S_{m'}| \geq L + R + 1$$

implying $|S_m \cap S_{m'}| \geq R$. For each $\ell \in S_m \cap S_{m'}$, the equality of representations implies $b_k^{(m)} = b_k^{(m')}$. Since this holds for any such pair S_m and $S_{m'}$, the subspace-restriction condition

in Theorem 1 must hold whenever $U \leq (L - R + 1)/2$, yielding identification as desired. \square

Proof of Theorem 2. Suppose that $\gamma \leq 1$. By iteratively using (S12) in Lemma S10, we have

$$\begin{aligned}
D_2(A_R^{k+1}) &\leq \gamma D_2(A_R^k) + \gamma h(J, \lambda_K) \\
&\leq \gamma(\gamma D_2(A_R^{k-1}) + \gamma h(J, \lambda_K)) + \gamma h(J, \lambda_K) \\
&\leq \dots \\
&\leq \gamma^{k+1} D_2(A_R^0) + \frac{\gamma}{(1-\gamma)} h(J, \lambda_K) \\
&\leq \gamma^{k+1} \|\mathbf{C}^*\|_2 + \frac{\gamma}{(1-\gamma)} h(J, \lambda_K).
\end{aligned}$$

Further, plugging the above inequality into (S9), it is easy to derive that

$$\begin{aligned}
\|\mathbf{C}^{k+1} - \mathbf{C}^*\|_2 &\leq \left(1 + \frac{\theta_{J,J} \text{tr}(K)}{c_-(J) \text{tr}(K + \lambda_K I)}\right) D_2(A^k) + h(J, \lambda_K) \\
&\leq \left(1 + \frac{\theta_{J,J} \text{tr}(K)}{c_-(J) \text{tr}(K + \lambda_K I)}\right) (\gamma^k \|\mathbf{C}^*\|_2) \\
&\quad + \left[\frac{\gamma}{(1-\gamma)} \left(1 + \frac{\theta_{J,J} \text{tr}(K)}{c_-(J) \text{tr}(K + \lambda_K I)}\right) + 1\right] h(J, \lambda_K).
\end{aligned}$$

Hence,

$$b_1 = 1 + \frac{\theta_{J,J} \text{tr}(K)}{c_-(J) \text{tr}(K + \lambda_K I)}, \quad b_2 = \frac{\gamma}{(1-\gamma)} \left(1 + \frac{\theta_{J,J} \text{tr}(K)}{c_-(J) \text{tr}(K + \lambda_K I)}\right) + 1. \quad (\text{S1})$$

The order of $h(J, \lambda_K)$ follows from Lemma S2. This completes the proof. \square

Proof of Theorem 3. This proof follows directly from the proof of Theorem 2 and Theorem 3 in the supplementary of Li et al. (2024) by replacing the functional covariate with the estimated functional covariate, and using Lemma S6,

$$M_3 = c_1 M_4^2 \delta_{\max}^2 \|\mathbf{B}^*\|_{\mathcal{K}}^2 + \sigma_x^2 n^{-1/2} M_4 \|\mathbf{B}^*\|_{\mathcal{K}}^2, \quad M_4 = n^{1/2} \lambda (2M_1 + 1) + \left(1 + \frac{1}{\sqrt{\nu_4}}\right) \sqrt{c_1} \text{tr}(T), \quad (\text{S2})$$

and we omit it here. \square

Proof of Theorem 4. Recall that $\mathcal{M}_{\hat{A}} = I_n - X_{\hat{A}}(X_{\hat{A}}X_{\hat{A}}^\top)^{-1}X_{\hat{A}}^\top$. According to the outcome model,

$$\mathcal{M}_{\hat{A}}Y = \mathcal{M}_{\hat{A}}X_{A^*}\beta_{A^*}^* + \mathcal{M}_{\hat{A}} \int_{\mathcal{T}} \hat{\mathbf{Z}}(t)\mathbf{B}^*(t)dt + \mathcal{M}_{\hat{A}}\hat{\nu},$$

where $\hat{\nu} = \int_{\mathcal{T}}(\mathbf{Z}(t) - \hat{\mathbf{Z}}(t))\mathbf{B}^*(t)dt + \epsilon$. By the definition of $\hat{\mathbf{F}}(t)$, under the null hypothesis that $\mathbf{B}^*(t) = 0$, we can obtain that

$$\begin{aligned} \sqrt{n}(T_n + \lambda I)^{-1}\hat{\mathbf{F}}(t) &= n^{-1/2}(K^{1/2}\hat{\mathbf{Z}}(t))^\top \mathcal{M}_{\hat{A}}Y = n^{-1/2}(K^{1/2}\hat{\mathbf{Z}}(t))^\top (\mathcal{M}_{\hat{A}}X_{A^*}\beta_{A^*}^* + \mathcal{M}_{\hat{A}}\epsilon) \\ &= n^{-1/2}(K^{1/2}\hat{\mathbf{Z}}(t))^\top \left((\mathcal{M}_{\hat{A}} - \mathcal{M}_{A^*})\epsilon + (\mathcal{M}_{\hat{A}} - \mathcal{M}_{A^*})X_{A^*}\beta_{A^*}^* + \mathcal{M}_{A^*}\epsilon \right) \\ &= S_1 + S_2 + S_3 \end{aligned}$$

where S_1, S_2, S_3 denote the above three terms, and the third equality follows from that $\mathcal{M}_{A^*}X_{A^*} = 0$.

We first calculate $\|S_1\|_2^2$. For any $\nu > 0$,

$$P(\|S_1\|_2^2 > \nu) \leq P(\|S_1\|_2^2 > \nu, \hat{A} = A^*) + P(\hat{A} \neq A^*) = 0$$

as $n \rightarrow \infty$. The inequality follows from that when $\hat{A} = A^*$, $\|S_1\|_2^2 = 0$ due to $\mathcal{M}_{\hat{A}} = \mathcal{M}_{A^*}$. Hence $\|S_1\|_2^2 = O_p(1)$. Similarly, $\|S_2\|_2^2 = O_p(1)$.

We first analyze its finite-dimensional distributions of S_3 . For any set of points t_1, t_2, \dots, t_m , consider the vector

$$n^{-1/2}(\epsilon^\top \mathcal{M}_{A^*}K^{1/2}\hat{\mathbf{Z}}(t_1), \dots, \epsilon^\top \mathcal{M}_{A^*}K^{1/2}\hat{\mathbf{Z}}(t_m))^\top = H\epsilon,$$

where $H = n^{-1/2}(\mathcal{M}_{A^*}K^{1/2}\hat{\mathbf{Z}}(t_1), \dots, \mathcal{M}_{A^*}K^{1/2}\hat{\mathbf{Z}}(t_m))^\top \in \mathbb{R}^{k \times n}$. Since ϵ_i are independent with mean 0 and variance σ^2 , the vector $H\epsilon$ has mean 0 and covariance matrix $Cov(H\epsilon) = \sigma^2 GG^\top$. Notice that by the law of large numbers, $n^{-1}HH^\top$ converges in probability to the matrix Σ

$$\Sigma_{ij} = n^{-1}K^{1/2}E(\tilde{\mathbf{Z}}^\top(t_i)\mathcal{M}_{A^*}\tilde{\mathbf{Z}}(t_j))K^{1/2}\sigma^2$$

by noticing that $|E(\tilde{\mathbf{Z}}^\top(t_i)\mathcal{M}_{A^*}\tilde{\mathbf{Z}}(t_j)) - E(\hat{\mathbf{Z}}^\top(t_i)\mathcal{M}_{A^*}\hat{\mathbf{Z}}(t_j))| = o(1)$ which is positive

definite. According to the multivariate central limit theorem, we can obtain that

$$H\epsilon \xrightarrow{d} N(0, \Sigma).$$

Next, we show the tightness of S_3 . Consider the term $\tilde{S}_3 = n^{-1/2} K^{1/2} \tilde{\mathbf{Z}}(t) \epsilon = n^{-1/2} \sum_{i=1}^n K^{1/2} \tilde{\mathbf{Z}}_i(t) \epsilon_i$.

Since

$$E \|K^{1/2} \tilde{\mathbf{Z}}_i(t) \epsilon_i\|_2^2 = \sigma^2 \int_{\mathcal{T}} \int_{\mathcal{T}} C(s, t) K(s, t) ds dt < \infty,$$

and $\{K^{1/2} \tilde{\mathbf{Z}}_i(t) \epsilon_i\}$ are independent and identically distributed random elements, then \tilde{S}_3 converges in distribution to a Gaussian process according to Theorem 7.7.6 of Hsing and Eubank (2015). It follows directly that \tilde{S}_3 is tight. Hence, S_3 is also tight by noticing that $\sup_t |K^{1/2} \tilde{\mathbf{Z}}(t) \mathcal{M}_{A^*} \epsilon| < \sup_t |K^{1/2} \tilde{\mathbf{Z}}(t) \epsilon|$.

According to limit of the finite-dimensional distributions in (S3) and the tightness of S_3 , Theorem 18.14 in Van der Vaart (2000) indicates that S_3 converges in distribution to a Gaussian process with the covariance

$$S_3 \xrightarrow{d} GP\left(0, n^{-1} K^{1/2} E(\tilde{\mathbf{Z}}^\top(s) \mathcal{M}_{A^*} \tilde{\mathbf{Z}}(t)) K^{1/2} \sigma^2\right).$$

By the Karhunen-Loeve expansion, the above Gaussian process G admits the decomposition $G = \sigma \sum_{j=1}^{\infty} \sqrt{\tilde{s}_j} \xi_j \psi_j$, where $\{\xi_j, j \geq 1\}$ are independent and identically distributed standard Gaussian random variables, $\psi_j, j \geq 1$ are orthogonal basis, and $\{\tilde{s}_j\}$ are eigen values of the operator $n^{-1/2} K^{1/2} E(\tilde{\mathbf{Z}}^\top(s) \mathcal{M}_{A^*} \tilde{\mathbf{Z}}(t)) K^{1/2}$. Hence,

$$\frac{\|S_3\|_2^2}{\sigma^2} \xrightarrow{d} \sum_{j=1}^{\infty} \tilde{s}_j \xi_j^2.$$

Combining the above results with $\|S_1\|_2^2 = O_p(1)$, $\|S_2\|_2^2 = O_p(1)$ and $\hat{\sigma}^2$ converge in probability to σ^2 by large law of numbers, we have

$$S_n \xrightarrow{d} \sum_{j=1}^{\infty} \tilde{s}_j \xi_j^2.$$

This completes the proof. □

S4 Auxiliary Lemmas

We first define some notations to facilitate our discussions. Recall that A_R^* is the true index set of the nonzero variables, \mathbf{C}^* is the true value of the scalar coefficients in the exposure model, and $\{A_R^k\}_k$ is the sequence of active sets generated by the FSDAR algorithm. For any given integers J and J_z^* with $J \geq J_z^*$ and $F \subset S$ with $|F| = J - J_z^*$, let $A^o = A_R^* \cup F$ and $I^o = (A^o)^c$. Define

$$D_2(A_R^k) = \|\mathbf{C}^*|_{A_R^* \setminus A_R^k}\|_2, \quad \Delta^k = \mathbf{C}^{k+1}|_{A_R^k} - \mathbf{C}^*|_{A_R^k}.$$

The term $D_2(A_R^k)$ measures the L_2 norm of the false zero coefficients in the k -th iteration, namely the coefficients in A_R^* but not in A_R^k . The term Δ^k measures the bias of the estimated coefficients in A_R^k .

Then, we let

$$\begin{aligned} A_1^k &= A_R^k \cap A^o, A_2^k = A^o \setminus A_1^k, I_3^k = A_R^k \cap I^o, I_4^k = I^o \setminus I_3^k, \\ A_{11}^k &= A_1^k \setminus (A^{k+1} \cap A_1^k), A_{22}^k = A_2^k \setminus (A^{k+1} \cap A_2^k), I_{33}^k = A^{k+1} \cap I_3^k, I_{44}^k = A^{k+1} \cap I_4^k. \end{aligned}$$

At the k -th iteration, the sets A_1^k and I_3^k contain the true and false positives in the active set A_R^k , respectively, while A_2^k and I_4^k contain the false and true negatives. The sets A_{11}^k and A_{22}^k include indices in A^o that will be removed in the next iteration, and I_{33}^k and I_{44}^k contain indices in I^o that will be added in the next iteration. Because the sparsity level in the algorithm is J , then $|A_R^k| = |A_R^{k+1}| = J$. Denote the cardinality of I_3^k by $\ell_k = |I_3^k|$. It is obvious that $A_R^k = A_1^k \cup I_3^k$, $A_2^k = |A^o| - |A_1^k| = |A^o| - (|A_R^k| - |I_3^k|) = J - (J - \ell_k) = \ell_k$. By definition,

$$|A_{11}^k| + |A_{22}^k| = |I_{33}^k| + |I_{44}^k|, \quad D_2(A^k) = \|\mathbf{C}^*|_{A^o \setminus A_R^k}\|_2 = \|\mathbf{C}^*|_{A_2^k}\|_2.$$

Lemma S1. *Letting A be the subset of \mathcal{S} with $|A| = J$, suppose that Assumption 2 holds,*

then

$$0 < nc_-(J)tr(K + \lambda_K I) \leq \|(\mathbf{X}_A^\top \mathbf{X}_A) \otimes (K_{\mathbf{u}}^\top K_{\mathbf{u}}) + \lambda I\|_{op} \leq nc_+(J)tr(K + \lambda_K I) < \infty, \quad (\text{S1})$$

$$0 < \frac{tr^{-1}(K + \lambda_K I)}{nc_-(J)} \leq \|[(\mathbf{X}_A^\top \mathbf{X}_A) \otimes (K_{\mathbf{u}}^\top K_{\mathbf{u}}) + \lambda I]^{-1}\|_{op} \leq \frac{tr^{-1}(K + \lambda_K I)}{nc_+(J)} < \infty \quad (\text{S2})$$

Proof. We first prove (S1). According to Lemma 7.2 of Alizadeh et al. (1998), the eigenvalue of the Kronecker product of two matrices is the product of the corresponding eigenvalues. By definition,

$$\begin{aligned} \|(\mathbf{X}_A^\top \mathbf{X}_A) \otimes (K_{\mathbf{u}}^\top K_{\mathbf{u}}) + \lambda I\|_{op} &= \sup_{h: \|h\|_{L_2}=1} |\langle [(\mathbf{X}_A^\top \mathbf{X}_A) \otimes (K_{\mathbf{u}}^\top K_{\mathbf{u}}) + \lambda I]h, h \rangle| \\ &\leq nc_+(J) \sup_{h: \|h\|_{L_2}=1} \left| \int (K(u, s) + \lambda I)h(s) ds \right| \leq nc_+(J)tr(K + \lambda I). \end{aligned}$$

Then it is easy to check that

$$nc_-(J)tr(K + \lambda I) \leq \|(\mathbf{X}_A^\top \mathbf{X}_A) \otimes K_{\mathbf{u}}^\top K_{\mathbf{u}} + \lambda I\|_{op} \leq nc_+(J)tr(K + \lambda I)$$

The derivation of (S2) follows directly. \square

Lemma S2. Suppose that Assumption 8 holds, then for any $\nu \in (0, 1/2)$,

$$P\left(h(J, \lambda_K) \leq \sigma_E \sqrt{J \log\left(\frac{p}{\nu}\right)} \sqrt{\frac{tr(K(K + \lambda I)^{-2})}{nm} + n^{-1} + J\sqrt{\lambda_K/2}}\right) \geq 1 - \nu, \quad (\text{S3})$$

where $h(J, \lambda_K) = \max_{|A|=J} \|(T_{nm}^A + \lambda_K I)^{-1}((nm)^{-1} \sum_i \sum_j E_i(u_j) K_{u_{ij}} X_{i,A} + \lambda_K \mathbf{C}_A^*)\|_2$ with T_{nm}^A being an opearator such that $T_{nm}^A(f) = (nm)^{-1} \sum_i \sum_j \langle X_{i,A}^\top f, K_{u_{ij}} \rangle_K K_{u_{ij}} X_{i,A}^\top$.

Proof. Recall that $X_j = (X_{1j}, \dots, X_{nj})^\top$, denote

$$\begin{aligned} h(J) &= \max_{|A| \leq T} \|((\mathbf{X}_A^\top \mathbf{X}_A) \otimes K_{\mathbf{u}}^\top K_{\mathbf{u}} + \lambda I)^{-1} \frac{1}{nm} \sum_{i=1}^n \sum_{j=1}^m K_{u_j} X_{ij} E_i(u_j)\|_{L_2} \\ &\leq \sqrt{|A|} \max_{j \in \{1, \dots, p\}} \|(\mathbf{X}_j^\top \mathbf{X}_j) \otimes K_{\mathbf{u}}^\top K_{\mathbf{u}} + \lambda I\|_{op}^{-1} \frac{1}{nm} \sum_{i=1}^n \sum_{j=1}^m K_{u_j} X_{ij} E_i(u_j)\|_{L_2} \\ &:= \sqrt{|A|} \max_{j \in \{1, \dots, p\}} \frac{1}{nm} G_j. \end{aligned}$$

Due to the fact $X_j^\top X_j = 1$, direct calculations lead to $\mathbb{E}(G_j) = 0$ and

$$\text{Var}(G_j) = \mathbb{E}\left[(K + \lambda_K I)^{-1} \frac{1}{nm} \sum_{i=1}^n \sum_{j=1}^m K_{u_j} X_{ij} E_i(u_j)\right]^2 = \sigma_E^2 \left(\frac{\text{tr}(K^2(K + \lambda_K I)^{-2})}{nm} + n \right) \quad (\text{S4})$$

following a similar spirit to (S6.8) in Li et al. (2025). As pointed out in Zhang (2005), $\text{tr}(K^2(K + \lambda_K I)^{-2}) \leq \text{tr}(K(K + \lambda_K I)^{-1})$ and the right right hand side term is simpler. Since $E_i(u_j)$ is sub-Gaussian, and by the union bound, for any $\nu \in (0, 1/2)$, we have

$$\mathbb{P}\left(\max_j \frac{1}{nm} G_j > t\right) \leq 2p \exp\left(-\frac{n^2 m^2 t^2}{2\text{Var}(G_j)}\right) \leq \nu,$$

where we take t as

$$t = \sqrt{4 \log(2p/\nu) \left[\sigma_E^2 \left((nm)^{-1} \text{tr}(K(K + \lambda_K I)^{-1}) + n^{-1} \right) \right]}.$$

For the bias term, denote $\{\kappa_k\}$ and $\{\phi_k(t)\}$ as the eigenvalues and eigenfunctions of the kernel K . For any ℓ , \mathbf{C}_ℓ^* admits the expansion $\mathbf{C}_\ell^*(t) = \sum_{k=1}^\infty \mathbf{C}_{\ell k}^* \phi_k(t)$ and $\sum_{k=1}^\infty \mathbf{C}_{\ell k}^{*2} / \kappa_k < \infty$ as \mathbf{C}_ℓ^* resides in the RKHS. It is easy to deduce that

$$\|\lambda_K(K + \lambda_K I)^{-1} \mathbf{C}_\ell^*\|_2^2 = \lambda_K \sum_{k=1}^\infty \frac{\lambda_K \kappa_k}{(\lambda_K + \kappa_k)^2} \frac{\mathbf{C}_{\ell k}^{*2}}{\kappa_k} \leq \frac{\lambda_K}{2} \sum_{k=1}^\infty \frac{\mathbf{C}_{\ell k}^{*2}}{\kappa_k} = \frac{\lambda_K}{2} \|\mathbf{C}_\ell^*\|_{\mathcal{K}}^2. \quad (\text{S5})$$

Recall that $|A| = J$, combining (S4) and (S5) we can derive that

$$\begin{aligned} h(J, \lambda_K) &= \max_{|A|=J} \|(T_{nm}^A + \lambda_K I)^{-1} ((nm)^{-1} \sum_i \sum_j E_i(u_j) K_{u_j} X_{i,A} + \lambda_K \mathbf{C}_A^*)\|_2 \\ &\leq h(J) + J \max_\ell \|\lambda_K(K + \lambda_K I)^{-1} \mathbf{C}_\ell^*\|_2 \\ &\leq \sqrt{J \log(p/\nu) \sigma_E^2 \left((nm)^{-1} \text{tr}(K(K + \lambda_K I)^{-1}) + n^{-1} \right)} + J \sqrt{\lambda_K/2}. \end{aligned}$$

This completes the proof. \square

Lemma S3. *Let C^\diamond be a coordinate-wise minimizer of the loss function with group L_0 penalty. Then, C^\diamond satisfies that*

$$d_\ell^\diamond = P_\ell^{-1} \check{\mathbf{X}}^\top (Z - \check{\mathbf{X}} C^\diamond) - nm \lambda_{\lambda_K} P_\ell^{-1} \Sigma C^\diamond, \text{ and } C^\diamond = H_\lambda(C^\diamond + d^\diamond), \quad (\text{S6})$$

where $H_\lambda(\cdot)$ is the hard thresholding operator that

$$(H_\lambda(C))_\ell = \begin{cases} 0, & \text{if } C_\ell^\top (P_\ell/nm) C_\ell < 2\lambda, \\ C_\ell, & \text{if } C_\ell^\top (P_\ell/nm) C_\ell \geq 2\lambda, \end{cases} \quad (\text{S7})$$

where $P_\ell = \check{X}_\ell^\top \check{X}_\ell + nm\lambda_K \Sigma$. Conversely, if C^\diamond and d^\diamond satisfy (S6), then C^\diamond is a local minimizer of (5).

Proof. Suppose C^\diamond is a coordinate-wise minimizer of L_λ in (5). Denote \check{X}_ℓ to be the ℓ -th column of $\check{\mathbf{X}}$. Then

$$\begin{aligned} C_\ell^\diamond &\in \arg \min_{t \in \mathbb{R}^m} \frac{1}{2nm} \|Z - \check{\mathbf{X}} C^\diamond - \check{X}_\ell(t + C_\ell^\diamond)\|^2 + \frac{\lambda_K}{2} t^\top \Sigma t + \lambda \|t^\top K(u)\|_0 \\ \Rightarrow C_\ell^\diamond &\in \arg \min_{t \in \mathbb{R}^m} \frac{1}{2nm} \left[t^\top (\check{X}_\ell^\top \check{X}_\ell + nm\lambda_K \Sigma) t - 2t^\top \check{X}_\ell^\top (\check{X}_\ell C_\ell^\diamond + Z - \check{X} C^\diamond) \right] + \lambda \|t^\top K(u)\|_0 \\ \Rightarrow C_\ell^\diamond &\in \frac{1}{2} \left[t - P_\ell^{-1} \check{X}_\ell^\top (\check{X}_\ell C_\ell^\diamond + Z - \check{X} C^\diamond) \right]^\top \frac{P_\ell}{nm} \left[t - P_\ell^{-1} \check{X}_\ell^\top (\check{X}_\ell C_\ell^\diamond + Z - \check{X} C^\diamond) \right] + \lambda \|C_\ell^\top K(t)\|_0. \end{aligned}$$

where $P_\ell = (\check{X}_\ell^\top \check{X}_\ell + nm\lambda_K \Sigma)$. By the definition of the hard thresholding operator, we have

$$C_\ell^\diamond = P_\ell^{-1} \check{X}_\ell^\top (\check{X}_\ell C_\ell^\diamond + Z - \check{X} C^\diamond) = C_\ell^\diamond - nm\lambda_K P_\ell^{-1} \Sigma C_\ell^\diamond + P_\ell^{-1} \check{X}_\ell^\top (Z - \check{X} C^\diamond) = H_\lambda(C_\ell^\diamond + d_\ell^\diamond),$$

which shows (S6) holds.

Conversely, suppose that (S6) holds. Let

$$A^\diamond = \{\ell \in S : (C_\ell^\diamond + d_\ell)^\top (P_\lambda/nm) (C_\ell^\diamond + d_\ell) \geq 2\lambda\}.$$

By (S6) and the definition of $H_\lambda(\cdot)$, we deduce that for $\ell \in A^\diamond$, $C_\ell^\diamond \top (P_\lambda/nm) C_\ell^\diamond \geq 2\lambda$. Furthermore, $d_{A^\diamond}^\diamond = 0$, which is equivalent to

$$C_{A^\diamond}^\diamond \in \arg \min \frac{1}{2nm} \sum_{i=1}^n \sum_{j=1}^m (\mathbf{Z}_i(t_j) - \sum_{l \in A^\diamond} X_{i\ell} K(t_{ij})^\top C_\ell)^2 + \frac{\lambda_K}{2} \sum_{l \in A^\diamond} C_\ell^\top \Sigma C_\ell.$$

Next we show that $L_\lambda(C^\diamond + h) \geq L_\lambda(C^\diamond)$ if h is small enough. We consider two cases. If

$h_{(A^\diamond)^c} \neq 0$, notice that $(C_\ell + h)^\top \Sigma (C_\ell + h) > C_\ell^\top \Sigma C_\ell$, then

$$\begin{aligned} L_\lambda(C^\diamond + h) - L_\lambda(C^\diamond) &\geq \frac{1}{2nm} \|\mathbf{Z} - \check{\mathbf{X}}C^\diamond - \check{\mathbf{X}}h\|_2^2 - \frac{1}{2nm} \|\mathbf{Z} - \check{\mathbf{X}}C^\diamond\|_2^2 + \lambda + \frac{\lambda_K}{2} \sum_\ell C_\ell \Sigma h \\ &\geq \lambda - |h^\top d^\diamond| \end{aligned}$$

is positive for sufficiently small h . If $h_{(A^\diamond)^c} = 0$, by the minimizing property of $C_{A^\diamond}^*$, we deduce that $L_\lambda(C^\diamond + h) \geq L_\lambda(C^\diamond)$. This complete the proof. \square

Lemma S4. *Suppose the conditions in Lemma S1 holds,*

$$\|\Delta^k\|_2 \leq \frac{\theta_{J,J} \text{tr}(K)}{c_-(J) \text{tr}(K + \lambda_K I)} \|C_{A_R^k}^*\|_2 + h(J, \lambda_K), \quad (\text{S8})$$

$$\|C^{k+1} - C^*\|_2 \leq \left(1 + \frac{\theta_{J,J} \text{tr}(K)}{c_-(J) \text{tr}(K + \lambda_K I)}\right) D_2(A^k) + h(J, \lambda_K), \quad (\text{S9})$$

where $h(J, \lambda_K) = \max_{|A|=J} \|(T_{nm}^A + \lambda_K I)^{-1}((nm)^{-1} \sum_i \sum_j E_i(u_j) K_{u_{ij}} X_{i,A} + \lambda_K C_A^*)\|_2$.

Proof. Denote $T_{nm}^{A_R^k}(f) = (nm)^{-1} \sum_i \sum_j \langle X_{i,A_R^k}^\top f, K_{u_{ij}} \rangle_{\mathcal{K}} K_{u_{ij}} X_{i,A_R^k}^\top$ and $h_{nm}^{A_R^k} = (nm)^{-1} \sum_i \sum_j Z_{ij} K_{u_{ij}} X_{i,A_R^k}$, where $X_{i,A_R^k} = (X_{i,\ell}, \ell \in A_R^k)^\top$.

Given the active set A_R^k at the k th iteration, the estimate at iteration $k+1$ is updated by minimizing the following loss function, leveraging the reproducing property $\langle C_{A_R^k}, K_{u_{ij}} \rangle_{\mathcal{K}} = C_{A_R^k}(u_{ij})$,

$$\frac{1}{nm} \sum_i \sum_j (Z_{ij} - X_{i,A_R^k}^\top \langle C_{A_R^k}, K_{u_{ij}} \rangle_{\mathcal{K}})^2 + \frac{\lambda_K}{2} \sum_{\ell \in A_R^k} \|C_\ell\|_{\mathcal{K}}^2,$$

By taking the Fréchet derivative of the loss function with respect to $C_{A_R^k}$, we obtain the estimate at iteration $k+1$,

$$\begin{aligned} C_{A_R^k}^{k+1} &= (T_{nm}^{A_R^k} + \lambda_K I)^{-1} h_{nm}^{A_R^k} = (T_{nm}^{A_R^k} + \lambda_K I)^{-1} (nm)^{-1} \sum_i \sum_j (X_{i,A_1^k} C_{A_1^k}^* + X_{i,A_2^k} C_{A_2^k}^* + E_i(u_j)) K_{u_{ij}} X_{i,A_R^k} \\ C_{A_R^k}^* &= (T_{nm}^{A_R^k} + \lambda_K I)^{-1} (T_{nm}^{A_R^k} + \lambda_K I) C_{A_R^k}^* = (T_{nm}^{A_R^k} + \lambda_K I)^{-1} (T_{nm}^{A_R^k} + \lambda_K I) C_{A_1^k}^* \\ &= (T_{nm}^{A_R^k} + \lambda_K I)^{-1} (nm)^{-1} \sum_i \sum_j \langle X_{i,A_1^k}^\top C_{A_1^k}^*, K_{u_{ij}} \rangle_{\mathcal{K}} K_{u_{ij}} X_{i,A_1^k}^\top + \lambda_K (T_{nm}^{A_R^k} + \lambda_K I)^{-1} C_{A_1^k}^*. \end{aligned}$$

According to Lemma S1, and the fact that $\|Tf\|_2 \leq \|T\|_{op} \|f\|_2$ for a linear operator T and

$f \in L_2(\mathcal{T})$, it follows

$$\begin{aligned} \|\Delta^k\|_2 &= \|\mathbf{C}_{A_R^k}^{k+1} - \mathbf{C}_{A_R^k}^*\|_2 = \left\| (T_{nm}^{A_R^k} + \lambda_K I)^{-1} \left((nm)^{-1} \sum_i \sum_j (X_{i,A_R^k}^k \mathbf{C}_{A_R^k}^* + E_i(u_j)) K_{u_{ij}} X_{i,A_R^k} + \lambda_K \mathbf{C}_{A_R^k}^* \right) \right\|_2 \\ &\leq \frac{\theta_{J,J} \text{tr}(K)}{c_-(J) \text{tr}(K + \lambda_K I)} \|\mathbf{C}_{A_R^k}^*\|_2 + h(J, \lambda_K), \end{aligned}$$

where $h(J, \lambda_K) = \max_{|A|=J} \|(T_{nm}^A + \lambda_K I)^{-1}((nm)^{-1} \sum_i \sum_j E_i(u_j) K_{u_{ij}} X_{i,A} + \lambda_K \mathbf{C}_A^*)\|_2$.

For the second inequality, according to the definition of A_2^k and by the triangle inequality, we have

$$\begin{aligned} \|\mathbf{C}^{k+1} - \mathbf{C}^*\|_2 &\leq \|\mathbf{C}_{A_R^k}^{k+1} - \mathbf{C}_{A_R^k}^*\|_2 + \|\mathbf{C}_{A^o \setminus A_R^k}^*\|_2 = \|\Delta^k\|_2 + \|\mathbf{C}_{A_R^k}^*\|_2 \\ &= \left(1 + \frac{\theta_{J,J} \text{tr}(K)}{c_-(J) \text{tr}(K + \lambda_K I)}\right) D_2(A_R^k) + h(J, \lambda_K). \end{aligned}$$

This completes the proof. \square

Lemma S5. *If the conditions in Lemma S1 holds, then*

$$\begin{aligned} D_2(A_R^{k+1}) &\leq \|\Delta_{A_{11}^k}^k\|_2 + \|\mathbf{C}_{A_{11}^k}^{k+1}\|_2 \\ &\quad + \frac{1}{c_-(J)} \left((2\theta_{J,J} + \lambda) \|\Delta_{A_R^k}^k\|_2 + \theta_{J,J} D_2(A_R^k) \right) + \frac{m}{c_-(J) \text{tr}(K + \lambda I)} (\|d_{A_{22}^k}^k\|_2 + h(J)), \end{aligned} \quad (\text{S10})$$

$$\|d_{I_{44}^k}^{k+1}\|_2 \leq (m^{-1} \text{tr}(K) \theta_{J,J} + \lambda) \|\Delta_{A_R^k}^k\|_2 + m^{-1} \text{tr}(K) \theta_{J,J} D_2(A_R^k) + h(J) + \lambda, \quad (\text{S11})$$

$$D_2(A_R^{k+1}) \leq \gamma D_2(A_R^k) + \gamma m h(J) / \theta_{J,J} \text{tr}(K + \lambda I) + \lambda. \quad (\text{S12})$$

Proof. According to Lemma 24 of Huang et al. (2018), we have

$$D_2(A_R^{k+1}) \leq \|\Delta_{A_R^k}^k\|_2 + \|\mathbf{C}_{A_{11}^k}^{k+1}\|_2 + \|\mathbf{C}_{A_{22}^k}^*\|_2. \quad (\text{S13})$$

Recall that $d_{A_{22}^k}^{k+1} = -(nm)^{-1} (X_{A_{22}^k}^\top \otimes K_{\mathbf{u}}^\top) [\mathbf{Z} - X_{A_R^k} \otimes K_{\mathbf{u}} \mathbf{C}_{A_R^k}^{k+1}] + \lambda \mathbf{C}_{A_{22}^{k+1}}$ and $\Delta_{A_R^k}^k = \mathbf{C}_{A_R^k}^{k+1} -$

$\mathbf{C}_{A_R^k}^*$, one can derive that

$$\begin{aligned}
& \|d_{A_{22}^k}^{k+1}\|_2 \\
&= \| (nm)^{-1} (X_{A_{22}^k}^\top \otimes K_{\mathbf{u}}^\top) [X_{A_R^k} \otimes K_{\mathbf{u}} \Delta_{A_R^k}^k + X_{A_R^k} \otimes K_{\mathbf{u}} \mathbf{C}_{A_R^k}^* - X_{A^o} \otimes K_{\mathbf{u}} \mathbf{C}_A^o - \mathbf{E}] + \lambda_K \mathbf{C}_{A_{22}^{k+1}} \|_2 \\
&= \| (nm)^{-1} (X_{A_{22}^k}^\top \otimes K_{\mathbf{u}}^\top) [X_{A_R^k} \otimes K_{\mathbf{u}} \Delta_{A_R^k}^k - X_{A_2^k} \otimes K_{\mathbf{u}} \mathbf{C}_{A_2^k}^* - \mathbf{E}] + \lambda_K \mathbf{C}_{A_{22}^{k+1}} \|_2 \\
&= \| (nm)^{-1} (X_{A_{22}^k}^\top \otimes K_{\mathbf{u}}^\top) [X_{A_R^k} \otimes K_{\mathbf{u}} \Delta_{A_R^k}^k - X_{A_{22}^k} \otimes K_{\mathbf{u}} \mathbf{C}_{A_{22}^k}^* - X_{A_2^k \setminus A_{22}^k} \otimes K_{\mathbf{u}} \mathbf{C}_{A_2^k \setminus A_{22}^k}^* - \mathbf{E}] + \lambda_K \mathbf{C}_{A_{22}^{k+1}} \|_2 \\
&\geq m^{-1} \text{tr}(K + \lambda_K I) \left(c_-(J) \|\mathbf{C}_{A_{22}^k}^*\|_2 - (\theta_{J,J} + \lambda) \|\Delta_{A_R^k}^k\|_2 - \theta_{J,J} \|\Delta_{A_R^k}^k\|_2 - \theta_{J,J} D_2(A_R^k) \right) - h(J),
\end{aligned}$$

where the first equality follows from the definition of d^{k+1} and \mathbf{Z} ; the second equality follows from the definition of Δ^k ; the third equality follows from simple algebra, and the last inequality follows from triangle inequality and the monotonicity property of $c_-(\cdot)$, $\theta_{a,b}$ and the definition of $h(J) = \max_{A \subset S: |A|=J} (nm)^{-1} \|(X_A^\top \otimes K_{\mathbf{u}}^\top) \mathbf{E}\|_2$. Plugging the above results into (S13), we have that (S10) holds.

Similarly, it is easy to deduce that for (S11),

$$\begin{aligned}
\|d_{I_{44}^k}^{k+1}\|_2 &= \| (nm)^{-1} (X_{I_{44}^k}^\top \otimes K_{\mathbf{u}}^\top) [X_{A_R^k} \otimes K_{\mathbf{u}} \Delta_{A_R^k}^k - X_{A_2^k} \otimes K_{\mathbf{u}} \mathbf{C}_{A_2^k}^* - \mathbf{E}] + \lambda_K (\mathbf{C}_{I_{44}^k} - \mathbf{C}_{I_{44}^k}^*) + \lambda_K \mathbf{C}_{I_{44}^k}^* \|_2 \\
&\leq m^{-1} \text{tr}(K + \lambda_K I) (\theta_{J,J} \|\Delta_{A_R^k}^k\|_2 + \theta_{J,J} D_2(A_R^k)) + h(J).
\end{aligned}$$

Similar to Lemma 25 and Lemma 26 of Huang et al. (2018), we have $\|\mathbf{C}_{A_{11}^k}^{k+1}\|_2 + \|d_{A_{22}^{k+1}}\|_2 \leq \sqrt{2} (\|\mathbf{C}_{I_{33}^k}^{k+1}\|_2 + \|d_{I_{44}^{k+1}}\|_2)$ and $\|\mathbf{C}_{I_{33}^k}^{k+1}\|_2 \leq \|\Delta_{I_{33}^k}^k\|_2$. It follows (S11) that

$$\begin{aligned}
& \|\Delta_{I_{33}^k}^k\|_2 + \|d_{I_{44}^{k+1}}\|_2 \leq \|\Delta^k\|_2 + \|d_{I_{44}^{k+1}}\|_2 \\
&\leq (m^{-1} \text{tr}(K + \lambda_K I) \theta_{J,J} + 1) \|\Delta^k\|_2 + m^{-1} \text{tr}(K + \lambda_K I) \theta_{J,J} D_2(A_R^k) + h(J).
\end{aligned}$$

It then follows that

$$\begin{aligned}
D_2(A_R^{k+1}) &\leq \left(\frac{2\theta_{J,J} + \lambda}{c_-(J)} + 1 \right) \|\Delta_{A_R^k}\|_2 + \frac{\theta_{J,J}}{c_-(J)} D_2(A_R^k) \\
&\quad + \frac{m}{c_-(J)tr(K + \lambda I)} h(J) + \max\left\{1, \frac{m}{c_-(J)tr(K + \lambda I)}\right\} (\|\mathbf{C}_{A_{11}^k}^{k+1}\|_2 + \|d_{A_{22}^k}^k\|_2) \\
&\leq \left(\max\left\{\sqrt{2}, \frac{m\sqrt{2}}{c_-(J)tr(K + \lambda I)}\right\} (m^{-1}tr(K + \lambda_K I)\theta_{J,J} + 1) + \left(\frac{2\theta_{J,J} + \lambda}{c_-(J)} + 1\right) \right) \|\Delta_{A_R^k}\|_2 \\
&\quad + \left(\max\left\{\sqrt{2}, \frac{m\sqrt{2}}{c_-(J)tr(K + \lambda I)}\right\} m^{-1}tr(K + \lambda_K I)\theta_{J,J} + \frac{\theta_{J,J}}{c_-(J)} \right) D_2(A_R^k) \\
&\quad + \left(\max\left\{\sqrt{2}, \frac{m\sqrt{2}}{c_-(J)tr(K + \lambda I)}\right\} + \frac{m}{c_-(J)tr(K + \lambda I)} \right) h(J)
\end{aligned}$$

According to (S8) that $\|\Delta_{A_R^k}\|_2 \leq \left(1 + \frac{\theta_{J,J}tr(K)}{c_-(J)tr(K + \lambda_K I)}\right) D_2(A^k) + h(J, \lambda_K)$, then

$$D_2(A_R^{k+1}) \leq \gamma D_2(A_R^k) + \gamma h(J, \lambda_K),$$

where

$$\begin{aligned}
\gamma &= \left(\max\left\{\sqrt{2}, \frac{m\sqrt{2}}{c_-(J)tr(K + \lambda I)}\right\} (m^{-1}tr(K + \lambda_K I)\theta_{J,J} + 1) + \left(\frac{2\theta_{J,J} + \lambda}{c_-(J)} + 1\right) \right) \\
&\quad \cdot \left(1 + \frac{\theta_{J,J}tr(K)}{c_-(J)tr(K + \lambda_K I)} \right). \tag{S14}
\end{aligned}$$

□

Lemma S6. *If the conditions in Assumptions 1-8 are satisfied, and data splitting is conducted such that the outcome model and the exposure model are estimated using different samples. For $T = K^{1/2}E(\tilde{\mathbf{Z}}(t)\tilde{\mathbf{Z}}(s))K^{1/2}$ and $T_n = K^{1/2}C_n(s, t)K^{1/2}$ with $C_n(s, t) = n^{-1/2} \sum_{i=1}^n \widehat{\mathbf{Z}}_i(s)\widehat{\mathbf{Z}}_i(t)$, then for any $\nu \in (0, 1)$*

$$\begin{aligned}
P\left(\|(T + \lambda I)^{-1/2}(T_n - T)\|_{op} \leq \left(1 + \frac{1}{\sqrt{\nu}}\right) \sqrt{\frac{c_1}{n}tr(T)tr(T(T + \lambda)^{-1})}\right) &\geq 1 - \nu, \\
P\left(\|(T_n - T)\|_{op} \leq \left(1 + \frac{1}{\sqrt{\nu}}\right) \sqrt{\frac{c_1}{n}tr^2(T)}\right) &\geq 1 - \nu.
\end{aligned}$$

Proof. Recall that by Mercer's Theorem, the operator kernel T admits the spectra decomposition $T(s, t) = \sum_{k=1}^{\infty} s_k \varphi_k(s)\varphi_k(t)$, where $s_1 > s_2 > \dots$ are eigenvalues of T , and $\{\varphi_k\}$ are

the eigenfunctions. Then for $h \in L_2(\mathcal{T})$, $\|h\|_{L_2} = 1$, one can have $h(t) = \sum_{k=1}^{\infty} h_k \varphi_k(t)$.

By definition, we can see that

$$\begin{aligned}
& \| (T + \lambda I)^{-1/2} (T_n - T) \|_{op} = \sup_{h: \|h\|_{L_2} = 1} | \langle (T + \lambda I)^{-1/2} h, (T_n - T) h \rangle | \\
&= \sup_{h: \|h\|_{L_2} = 1} \sum_{j,k} \frac{h_j h_k}{(s_j + \lambda)^{1/2}} \langle \varphi_j, (T_n - T) \varphi_k \rangle \\
&\leq \sup_{h: \|h\|_{L_2} = 1} \left(\sum_{j,k} h_j^2 h_k^2 \right)^{1/2} \left(\sum_{j,k} \frac{1}{s_j + \lambda} \langle \varphi_j, (T_n - T) \varphi_k \rangle^2 \right)^{1/2} \\
&\leq \left(\sum_{j,k} \frac{1}{s_j + \lambda} \langle \varphi_j, (T_n - T) \varphi_k \rangle^2 \right)^{1/2} := H_n,
\end{aligned}$$

where H_n corresponds to the last term.

Denote $\tilde{C}_n(s, t) = n^{-1/2} \sum_{i=1}^n \tilde{\mathbf{Z}}_i(s) \tilde{\mathbf{Z}}_i(t)$ and $\tilde{T}_n = K^{1/2} \tilde{C}_n K^{1/2}$, Take the expectation of H_n , then

$$\begin{aligned}
E(H_n) &\leq \left(\sum_{j,k} \frac{1}{s_j + \lambda} E \langle \varphi_j, (T_n - T) \varphi_k \rangle^2 \right)^{1/2} \\
&= \left(\sum_{j,k} \frac{1}{s_j + \lambda} E \langle \varphi_j, (T_n - \tilde{T}_n) \rangle^2 \right)^{1/2} + \left(\sum_{j,k} \frac{1}{s_j + \lambda} E \langle \varphi_j, (\tilde{T}_n - T) \varphi_k \rangle^2 \right)^{1/2} \\
&= H_{n1} + H_{n2},
\end{aligned}$$

where H_{n1} and H_{n2} denote the above two terms, respectively.

Direct calculations lead to

$$\begin{aligned}
E\langle \varphi_j, (T_n - \tilde{T}_n)\varphi_k \rangle^2 &= E\left(\int_{\mathcal{T}} \int_{\mathcal{T}} K^{1/2} \varphi_j(s) (C_n(s, t) - \tilde{C}_n(s, t)) K^{1/2} \varphi_k(t) ds dt\right)^2 \\
&= \frac{1}{n} E\left(\int_{\mathcal{T}} \int_{\mathcal{T}} K^{1/2} \varphi_j(s) [\tilde{\mathbf{Z}}(s) \tilde{\mathbf{Z}}(t) - \tilde{\mathbf{Z}}(s) \tilde{\mathbf{Z}}(t)] K^{1/2} \varphi_k(t) ds dt\right)^2 \\
&= \frac{1}{n} E\left(\int_{\mathcal{T}} \int_{\mathcal{T}} K^{1/2} \varphi_j(s) [X_i^\top \tilde{\mathbf{C}}(t) \tilde{\mathbf{C}}^\top(s) X_i - X_i^\top \mathbf{C}(t) \mathbf{C}^\top(s) X_i] K^{1/2} \varphi_k(t) ds dt\right)^2 \\
&= \frac{1}{n} E\left(\int_{\mathcal{T}} \int_{\mathcal{T}} K^{1/2} \varphi_j(s) X_i^\top [(\tilde{\mathbf{C}}(t) - \mathbf{C}(t)) (\tilde{\mathbf{C}}(s) - \mathbf{C}(s))^\top + 2(\tilde{\mathbf{C}}(t) - \mathbf{C}(t)) \mathbf{C}^\top(s)] X_i K^{1/2} \varphi_k(t) ds dt\right)^2 \\
&= \frac{1}{n} E\left(\int_{\mathcal{T}} \int_{\mathcal{T}} K^{1/2} \varphi_j(s) \tilde{\mathbf{Z}}(s) [(\frac{\tilde{\mathbf{C}}(t) - \mathbf{C}(t)}{\mathbf{C}(t)})(\frac{\tilde{\mathbf{C}}(s) - \mathbf{C}(s)}{\mathbf{C}(s)})^\top + 2(\frac{\tilde{\mathbf{C}}(t) - \mathbf{C}(t)}{\mathbf{C}(t)})] \tilde{\mathbf{Z}}(t) K^{1/2} \varphi_k(t) ds dt\right)^2 \\
&\leq \frac{1}{n} E^{1/2} \left(\int_{\mathcal{T}} \int_{\mathcal{T}} K^{1/2} \varphi_j(t) \tilde{\mathbf{Z}}(t) dt\right)^4 E^{1/2} \left(\int_{\mathcal{T}} \int_{\mathcal{T}} K^{1/2} \varphi_k(t) \tilde{\mathbf{Z}}(t) dt\right)^4 \\
&\leq \frac{c_1}{n} E\left(\int_{\mathcal{T}} \int_{\mathcal{T}} K^{1/2} \varphi_j(t) \tilde{\mathbf{Z}}(t) dt\right)^2 E\left(\int_{\mathcal{T}} \int_{\mathcal{T}} K^{1/2} \varphi_k(t) \tilde{\mathbf{Z}}(t) dt\right)^2,
\end{aligned}$$

where the first inequality follows from that $\sup_t (\tilde{\mathbf{C}}(t) - \mathbf{C}(t)) / \mathbf{C}(t) = o_p(1)$ due to $\|\tilde{\mathbf{C}}(t) - \mathbf{C}(t)\|_2^2 = o_p(1)$, and the last inequality follows directly from Assumption 3. It is obvious that $E\left(\int_{\mathcal{T}} \int_{\mathcal{T}} K^{1/2} \varphi_j(t) \tilde{\mathbf{Z}}(t) dt\right)^2 = \langle T\varphi_j, \varphi_j \rangle = s_j$, then

$$E\langle \varphi_j, (T_n - \tilde{T}_n)\varphi_k \rangle^2 \leq c_1 s_j s_k / n.$$

Hence, we obtain that

$$\begin{aligned}
E(H_{n1}) &\leq \left(\frac{c_1}{n}\right)^{1/2} \left(\sum_{j,k} \frac{s_j s_k}{s_j + \lambda}\right)^{1/2} = \left(\frac{c_1}{n}\right)^{1/2} \left(tr(T) tr(T(T + \lambda I)^{-1})\right)^{1/2}, \\
E(H_{n1}^2) &\leq \frac{c_1}{n} tr(T) tr(T(T + \lambda I)^{-1}).
\end{aligned}$$

According to the concentration inequity that

$$P(|H_{n1} - EH_{n1}| \geq t) \leq \frac{EH_{n1}^2}{t^2},$$

taking $t = \frac{1}{\sqrt{\nu}} \sqrt{c_1 tr(T) tr(T(T + \lambda I)^{-1}) / n}$, we have

$$P\left(H_{n1} \geq (1 + \frac{1}{\sqrt{\nu}}) \sqrt{\frac{c_1}{n} tr(T) tr(T(T + \lambda I)^{-1})}\right) \leq \nu.$$

Similarly, we can show that

$$P\left(H_{n2} \geq (1 + \frac{1}{\sqrt{\nu}})\sqrt{\frac{c_1}{n} \text{tr}(T)\text{tr}(T(T + \lambda)^{-1})}\right) \leq \nu.$$

Then it follows with probability at least $1 - \nu$,

$$\|(T + \lambda I)^{-1/2}(T_n - T)\|_{op} \leq H_n \leq (1 + \frac{1}{\sqrt{\delta}})\sqrt{\frac{c_1}{n} \text{tr}(T)\text{tr}(T(T + \lambda)^{-1})}.$$

Hence, (S15) holds. By similar steps, we can prove that (S15) holds and we omit here. \square

References

Alizadeh, F., J.-P. A. Haeberly, and M. L. Overton (1998). Primal-dual interior-point methods for semidefinite programming: convergence rates, stability and numerical results. *SIAM Journal on Optimization* 8(3), 746–768.

Hsing, T. and R. Eubank (2015). *Theoretical foundations of functional data analysis, with an introduction to linear operators*, Volume 997. John Wiley & Sons.

Huang, J., Y. Jiao, Y. Liu, and X. Lu (2018). A constructive approach to l_0 penalized regression. *The Journal of Machine Learning Research* 19(1), 403–439.

Li, T., Y. Yu, J. Marron, and H. Zhu (2024). A partially functional linear regression framework for integrating genetic, imaging, and clinical data. *The Annals of Applied Statistics* 18(1), 704–728.

Li, T., Y. Yu, X. Wang, J. Marron, and H. Zhu (2025). Semi-nonparametric varying coefficients models for imaging genetics. *Statistica Sinica (Accepted)*.

Van der Vaart, A. W. (2000). *Asymptotic statistics*, Volume 3. Cambridge university press.

Zhang, T. (2005). Learning bounds for kernel regression using effective data dimensionality. *Neural computation* 17(9), 2077–2098.